The Design and Experimental Investigation of an Alumina Reticulate Porous Ceramic Heat Exchanger for High Temperatures

A Thesis
SUBMITTED TO THE FACULTY OF
UNIVERSITY OF MINNESOTA
BY

Aayan Banerjee

IN PARTIAL FULFILLMENT OF THE REQUIREMENTS
FOR THE DEGREE OF
MASTER OF SCIENCE

Dr. Jane H. Davidson, Adviser

June 2014

Acknowledgements

I would like to thank my parents for their faith and support throughout my academic career. To my brother, thank you for inspiring me and guiding me during my formative years and for always keeping me focused on the path of knowledge and discovery.

My heartfelt thanks to my advisor, Dr. Jane H. Davidson, for giving me the opportunity to participate in such intriguing research in an avant-garde and highly important field. Thanks to Dr. Terrence Simon, Dr. Allison Hubel and Dr. Thomas Chase for all of their encouragement during my time in graduate school. I would also like to thank all of my colleagues in the Solar Lab, especially, Rohini Bala Chandran, Peter T. Krenzke, Dr. Brandon J. Hathaway and Dr. Luke J. Venstrom for their constant critique and guidance.

To my friends, Adam Gladen, Zofia Kaminski, Jon Andri Hjaltason, Pieter Custers, Malachi Cook, Robert De Smith and Jerome Kessler, all I can say is that I am humbled by the love and kinship that we have shared over the past two years. Thank you for all the memories!

The financial support by the U.S. Department of Energy's Advanced Research Projects Agency-Energy (award no. DE-AR0000182) to the University of Minnesota is gratefully acknowledged.

Dedication

To my friends,

Bob and Jerry

Abstract

The sensible heating of sweep gas and oxidizer is a considerable energy sink in the isothermal splitting of carbon dioxide (CO_2) and water vapor (H_2O) using the solar thermochemical non-stoichiometric reduction and oxidation of ceria. Efficient gas phase heat recovery is critical to improving cycle efficiencies. However, operating temperatures of 1773 K provide a major hurdle in realizing high levels of heat recovery. The present study focuses on the design, modeling and testing of an alumina heat exchanger filled with reticulate porous ceramic (RPC). The heat exchanger has been designed to operate reliably at temperatures up to 1773 K, integrate seamlessly with the reactor designed for isothermal CO_2 and H_2O splitting using ceria and obtain an effectiveness of >0.85 for the range of flow rates anticipated during operation of the isothermal reactor. The RPC morphology, namely porosity and pore density and the geometry of the heat exchanger are selected based on the results of a fluid flow and heat transfer model of the heat exchanger. Results indicate that a concentric tube-in-tube counterflow alumina RPC filled heat exchanger yields an effectiveness >0.9 and leads to a projected reactor efficiency of 2.8%. The outer alumina tube has an o.d. of 69.9 mm and i.d. of 63.6 mm and the inner alumina tube has an o.d. of 44.4 mm and an i.d. of 38.1 mm. The heat exchanger is 1.4 m long and is filled with 85% porous, 10 ppi alumina RPC. The performance of a shorter 0.4 m long prototype at temperatures up to 1240 K is investigated experimentally. Heat transfer measurements were made at two hot inlet temperatures of 600 K and 1240 K by combusting methane in air. The cold inlet temperature was constant at 300 K. The overall heat transfer coefficient, effectiveness and pressure drop were measured for a fixed hot stream flow rate of CH_4+air of 1.7×10^{-2}

mol s^{-1} and cold stream flow rates of N_2 in the range 1.8×10^{-2} to 2.7×10^{-2} mol s^{-1}. The results show that the heat exchanger with a high specific surface area of 917 m^{-1} obtained overall heat transfer coefficients in the range 26 to 32 W m^{-2} K^{-1} at 600 K and 36 to 41 W m^{-2} K^{-1} at 1240 K for the range of operating conditions tested. Cold side heat exchanger effectiveness values of up to 0.73 were obtained with low pressure drops up to 1023 Pa at hot stream molar flow rate of 1.7×10^{-2} mol s^{-1} and cold stream molar flow rate of 2.7×10^{-2} mol s^{-1} and thermal duties of 450 W.

Table of Contents

List of Tables

List of Figures

Nomenclature

Latin

a	inner radius of inner cylinder, mm
$\tilde{a}$	specific surface area, m^{-1}
A	area, m^2
A_r	cross-sectional area ratio
b	channel permeability, m^2, or inner radius of collar, mm
c	outer radius of collar, mm
c_p	specific heat of gas at constant pressure, J kg^{-1} K^{-1}
c_v	specific heat of gas at constant volume, J kg^{-1} K^{-1}
C	concentration ratio
C_F	dimensionless inertial coefficient
d, D	diameter, m
d_h	hydraulic diameter, m
E	elastic modulus, GPa
F	inertial coefficient, m^{-1}
F_L	fraction of absorbed solar input lost due to convection and conduction through reactor insulation
h_c	convection coefficient, W m^{-2} K^{-1}
$\bar{h}$	average heat transfer coefficient, W m^{-2} K^{-1}
$\bar{H}$	average enthalpy of gas, J
ΔH_r	molar reaction enthalpy for fuel production, J mol^{-1}
HHV	higher heating value, J mol^{-1}
I	solar constant, W m^{-2}
k	thermal conductivity, W m^{-1} K^{-1}
k_k	Cozeny constant
K	permeability of open cell foam, m^2
K_{eq}	equilibrium rate constant

l	length, m
L	length of heat exchanger, m
m	mass, kg
$\dot{m}$	mass flow rate, kg s^{-1}
M	total number of temperature measurements by a thermocouple
n	total number of thermocouples at a point of interest
$\dot{n}$	molar gas flow rate, mol s^{-1}
$\bar{\dot{n}}'_f$	average rate of fuel production per unit mass of ceria, mol kg^{-1} s^{-1}
Nu	Nusselt number
NTU	number of heat transfer units
p	pressure, Pa, or pumping power per unit mass of ceria, W g $ceria^{-1}$
P	dimensionless pressure drop
ppi	pores per inch
Pr	Prandtl number
q	energy per unit mass of ceria, J kg^{-1}
$\dot{Q}$	heat transfer rate, W
r	primary radial coordinate, m
R	radius, m
R_{th}	thermal resistance, K W^{-1}
Re	Reynolds number
$\bar{T}$	bulk mean gas temperature, K
T_R	temperature of reactor cavity, K
u	gas velocity in axial direction
U	overall heat transfer coefficient, W m^{-2} K^{-1}, or dimensionless velocity
$\vec{V}$	gas velocity vector
$\dot{V}$	volume flow rate of gas, m^3 s^{-1}
x	primary axial coordinate, m, or mole fraction

Greek

β	extinction coefficient, m^{-1}
Δ	change in respective quantity
δ	deformation or interference, mm, or ceria non-stoichiometry
ε	heat exchanger effectiveness or emissivity
ϕ	porosity
γ	ratio of gas specific heats (c_p/c_v)
∇	gradient of vector
η	reactor efficiency, %
η_{pump}	isentropic pumping efficiency
ρ	density of gas, kg m^{-3}
σ	Stefan-Boltzmann constant, W m^{-2} K^{-4}, or stress, Pa
ψ	dimensionless radial coordinate
τ	duration, s
μ	viscosity of gas, kg m^{-1} s^{-1}, or Poisson's ratio

Subscripts

1	inner surface of inner tube of heat exchanger or hot inlet wall
2	outer surface of inner tube of heat exchanger or hot outlet wall
3	inner surface of outer tube of heat exchanger or cold inlet wall
4	cold outlet wall
an	pertaining to the annulus
b	base of thermocouple
c	pertaining to the cold stream of heat exchanger
corr	corrected quantity
ceria	pertaining to ceria
chem	pertaining to the water splitting or carbon dioxide splitting reaction

dry	pertaining to dry stream
eff	effective
f	pertaining to fluid or fuel
g	pertaining to gas
fe	effective fluid phase property of porous media
h	pertaining to hot stream of heat exchanger
i	inlet or species index
j	for element ‘j’ or pertaining to thermocouple junction
lm	pertaining to log mean
loss	pertaining to losses to the ambient
LFE	pertaining to the laminar flow element
m	mean
min	minimum
o	outlet or outer cylinder
ox	oxidizer or pertaining to oxidation
p	pore-scale
pump	pertaining to pump
r	pertaining to the radial direction
rd	pertaining to reduction
rad	pertaining to radiation
rel	relative to dry air
s	pertaining to solid
se	effective solid phase property of porous media
sf	solid to fluid
sg	sweep gas
solar	pertaining to solar power
spatial	pertaining to spatial variations
st	strut

t	pertaining to the tube or tangential
tot	total
w	tube wall

Superscripts

′	per unit mass of ceria
–	average

Chapter 1

Introduction

The splitting of carbon dioxide and water vapor to produce syngas, a mix of CO and H_2, is a promising method of storing solar energy. In the context of this study, the 'isothermal' non-stoichiometric redox cycling of ceria is of particular interest and has been discussed in [1-3]. The splitting of water vapor and carbon dioxide occurs in two steps, namely, reduction and oxidation. During reduction, the ceria releases oxygen atoms from its crystal lattice in an environment with a low partial pressure of oxygen. On passing an oxidizer like CO_2 or H_2O, the reduced ceria removes oxygen atoms from the oxidizer and thereby reduces CO_2 or H_2O to CO or H_2 respectively. In the 'isothermal' cycle, the temperature of the ceria bed is kept constant over the entire redox cycle. The isothermal cycle has several advantages over the two-temperature cycle namely, the elimination of the requirement for solid phase heat recovery and the absence of thermal stresses due to temperature gradients in the ceria and other construction materials in the reactor. However, based on the thermodynamics of ceria [4], the isothermal cycle engenders a much lower driving potential for fuel production than the two-temperature cycle thereby necessitating much lower partial pressures of oxygen during reduction to produce an equivalent amount of fuel. A commonly used technique to drive down the oxygen partial pressure during reduction is sweeping the reactor with an inert gas.

Our group at the University of Minnesota's High Temperature Solar Laboratory has designed a reactor to maximize the process efficiency for the isothermal solar thermochemical splitting of CO_2 and H_2O using ceria. The reactor comprises of a solar

cavity receiver which contains 6 tubular reactive elements lined along the circumference. Figure 1 is a cross-sectional view of the reactor. The reactive element consists of two concentric high density, high purity (99.8%) alumina tubes. The outer tube has an outer diameter, o.d. of 69.8 mm and an inner diameter of 63.6 mm and is closed at one end. The inner tube has an o.d. of 44.4 mm and an i.d. of 38.1 mm. The reactant gas stream enters through the inner tube, reverses direction and flows out over the reactive ceria pellets (~4 mm diameter) in the annular gap. The reactive elements are housed in a 299.2 mm diameter, 347 mm long cavity with a 35.6 mm diameter aperture to reach temperatures up to 1773 K in the ceria pellet bed using the incident solar radiation of up to 3 kW.

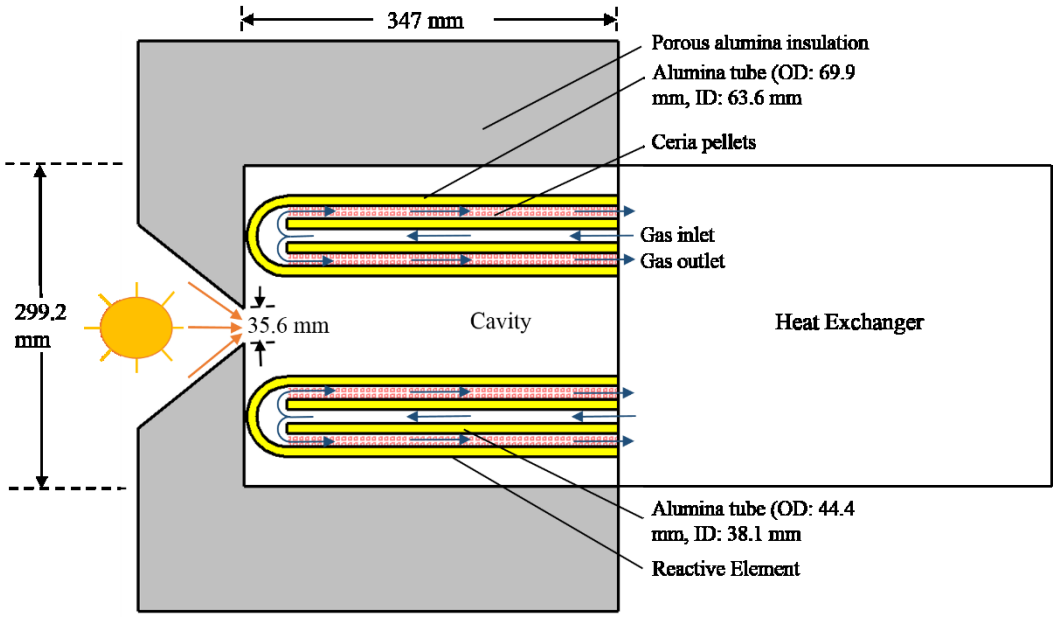

Figure 1. Cross-section view of the solar thermochemical reactor showing the reactor cavity and reactive elements. The arrows indicate direction of gas flow. The figure is not to scale.

An energy balance on the reactor cavity gives,

$$\dot{Q}_{solar} = \dot{Q}_{chem} + \dot{Q}_{loss} + \dot{Q}_{g} \qquad (1.1)$$

The term on the left hand side is the amount of solar energy entering the cavity. The first term on the right hand side is the reaction energy associated with the splitting of CO_2 or H_2O. The following term includes all the thermal losses from the cavity including reradiation and natural convection losses out the aperture and losses through the insulation due to conduction and convection. The final term on the right hand side represents the sensible heat required to raise the gas temperature from the inlet temperature to the reactor temperature (=1773 K). Based on the analysis in [1,2], the energy required for sensible heating is found to be significant especially when using sweep gas during reduction as is the case here. To obtain high process efficiencies it is imperative to preheat the inlet gas stream by effectively recuperating the heat of the effluent stream exiting the reactor at 1773 K. Based on a thermodynamic analysis, Bader et al. [1] estimates that heat exchanger effectiveness of >0.9 is required to obtain solar-to-fuel efficiencies of >5 %. Venstrom et al. [2] used experimental data to project reactor efficiencies for various heat exchanger effectiveness. The analysis shows that the reactor efficiency improves by an order of magnitude from <0.5% to 3.7% as the level of heat recuperation increases from 0 to 0.9. These analyses underscore the importance of a highly effective gas-phase heat exchanger capable of operating at temperatures up to 1773 K.

The major challenges in designing such a heat exchanger are the high operating temperatures and the ability to integrate the heat exchanger with the reactor including making gas-tight connections at 1773 K whilst still obtaining high values of effectiveness. Operating temperatures of 1773 K limit the materials of construction to refractory ceramics like alumina (Al_2O_3) and silicon carbide (SiC) and designs of gas-

tight ceramic-ceramic joints at 1773 K are limited to diffusion bonding or shrink-fitting [5].

In the present work, the capability of a counterflow alumina RPC filled heat exchanger is analyzed. The thesis is organized to guide the reader through the approach taken to design, model and test the heat exchanger capable of reliably operating at temperatures up to 1773 K and obtaining a heat recovery effectiveness of >0.85 for the range of flow rates to be used during reactor operation. Chapter 2 contains a review of the literature on the modeling approaches used in prior work to analyze fluid flow and heat transfer through porous media. Chapter 3 describes the design and methods used to model the heat exchanger in order to optimize foam morphology and geometry of the heat exchanger. Chapter 4 is written in a journal paper format and reports an experimental study conducted to evaluate the performance of a prototype heat exchanger. Finally, chapter 5 concludes the thesis with a summary of the key findings and recommendations for future work.

Chapter 2

Literature Review

The use of open cell foams in heat exchangers is very promising [6-7] due to higher specific surface areas, in the range of 500 – 10,000 m^{-1} for compressed metal foams [8], a conductive solid matrix and a more tortuous path for the working fluid which promotes mixing. However, the maximum operating temperatures for state-of-the-art superalloys is limited to 1123 K due to creep formation [5]. Therefore, ceramic open cell foams are required for operating temperatures up to 1773 K as is the case with many solar thermochemical processes.

The fluid flow and heat transfer through open cell foams need to be modeled to select the foam morphology namely foam porosity and pore density along with foam material to maximize heat transfer and minimize pressure drop. Several analytical [9-13] and numerical [14-17] models have been published in the literature which model thermal and fluid transport through open cell foams as forced convective heat transfer through a porous medium using volume averaged effective properties for the medium. The models were verified against experiments conducted primarily with metal foams [18-20]. Lu et al [12] and Zhao et al. [13] derived an analytical solution to solve the volumetric mass, momentum and energy transport equations in a tube-in-tube foam filled heat exchanger. The Brinkman extended Darcy model was solved for momentum transport and the local thermal non-equilibrium approach was used to model the energy transport. It is important to note that the Dupuit-Forchheimer term which accounts for the pressure drop due to inertial effects was neglected. Vafai and Kim [17] have shown that inertial effects can

have a significant impact on the pressure drop for highly permeable media like foams when the pore scale Re>0.1.

The accuracy of any analytical and numerical model depends heavily on the determination of effective transport properties for the foam namely, permeability, inertial coefficient, interfacial heat transfer coefficient and effective thermal conductivity. The permeability and inertial coefficient for fluid flow through porous ceramic foam depend on the geometric characteristics of the foam. Bhattacharya et al. [10] improved the analytical expression obtained by Du Plessis et al. [21] for permeability and inertial coefficient by noting that the flow through metal foams is analogous to flow over bluff bodies. The improved model correlated well with experimental data obtained by Bhattacharya [10] for aluminum and reticulated vitreous carbon (RVC) foams having porosity in the range of 94 – 97% and pore density in the range of 5 – 40 pores per inch (ppi). Petrasch et al. [22] computed the permeability and inertial coefficient for a pore-scale Re range of 0.2 – 200 by performing direct pore-level numerical solutions (DPLS) on 3-D digital representations of a 86% porous, 10 ppi SiC foam sample obtained by X-ray tomography. Comparing the results with existing flow models for porous media, Petrasch concluded that the Karman-Cozeny equation, with a deviation of 15%, and the Ergun equation, with a deviation of 12%, provided the best estimates of permeability and inertial coefficient respectively.

Petrasch [22] also estimated the interfacial heat transfer coefficient by proposing a Nu correlation for pore-scale Re in the range of 0.2 – 200, Pr in the range 0.1 – 10 and Pe>1. The correlation was derived based on the DPLS results and was in good agreement with the experimental results obtained by Younis and Viskanta [20].

There are several models which have been proposed to estimate the effective conductivity (k_e) of porous media. The series model approximates k_e by considering the fluid to pass through two distinct regions. The first consists solely of the fluid phase and the second comprises purely of the solid phase. The volumes of the regions are given by the volume fractions of the two phases. The parallel model approximates k_e by considering the fluid to pass through the two distinct regions simultaneously. The series and parallel models are simplistic models used to determine k_e and serve to provide the lower and upper bounds respectively. They do not represent the structure of any physical porous foam.

The effective conductivity has a strong dependence of the foam structure and the foam aspect ratio defined as the ratio of the length to the diameter of the struts [23]. Several cubic unit cell models [24-28] were developed to calculate k_e. The unit cell considered for 1-D conduction analysis is some variation of a solid cube with a cubic or spherical void, arranged either in an in-line or staggered combination. According to Coquard et al. [16] and Kamiuto [29], the Schuetz-Glicksman model [28], developed for polyurethane foams, has the best fit with the available experimental data (±30%) for high porosity (φ>90%) metal foams obtained by Calmidi and Mahajan [23] and Zhao et al. [30].

Amongst the analytical models specifically developed for open cell porous foams [23, 31, 32], the model developed by Bhattacharya et al. [32] which idealizes the cellular morphology of the open cell porous foam into a 2-D representation of hexagonal struts and circular intersection nodes, has the best fit with the experimental data obtained by Calmidi and Mahajan [23] and direct numerical simulations (DNS) of pore-scale

conduction heat transfer performed by Petrasch et al. [33]. Petrasch simulated conduction heat transfer in 3-D digital representations of two specimens of 10 ppi Rh-catalyst coated SiC foam obtained by high resolution X-ray tomography. The first specimen had a nominal porosity of 81% and the second had a nominal porosity of 90%. The results of Bhattacharya's analytical model and the DNS results agreed to within 4% of each other.

Experiments conducted by Zhao et al. [30] show that the effective solid thermal conductivity of a 30 ppi, 90% porous steel alloy (FeCrAlY) foam can be significantly higher at 803 K as compared to room temperature measurements due to radiation. Loretz et al. [34] have summarized the various analytical models for estimating the radiative properties of various foam structures. To obtain accurate results using the analytical models, the extinction coefficient (β) and the scattering albedo (ω) are important properties which need to be evaluated. Hendricks and Howell [35] evaluated β and ω for 10, 20 and 65 ppi zirconia (ZrO_2) and SiC RPCs using experimental measurements of the spectral hemispherical reflectance and transmittance across the wavelength range 0.4 – 5 μm. The results were used to adjust the empirical parameter in the correlation for β developed by Hsu and Howell [36] based on geometrical optics. Petrasch et al. [37] applied the Monte-Carlo ray-tracing technique to evaluate β for a 3-D digital representation of a 90% porous, 10 ppi SiC obtained by high resolution X-ray tomography. The results were found to be in good agreement with the experimental results obtained by Hendricks and Howell.

The Rosseland diffusion approximation and the P_1 approximation are two approaches to modeling radiative transfer which greatly decrease computational time. Hottel and Sarofim [38] have shown that the Rosseland diffusion approximation is valid

when the medium absorbs and scatters radiation isotropically. However, experimental measurements by Glicksmann et al. [39] have shown scattering in foams to be highly anisotropic. Glicksmann recommends that to apply Rosseland, the foam must be 'optically thick'. The 'optical thickness' (τ_L) is a dimensionless parameter which is equal to the product of the extinction coefficient and the optical path length. Hischier et al. [40] used both approaches to evaluate the volumetric radiative flux for 81% porous, 10 ppi RPC concentrically lined by two cylinders. The optical thickness was ~3. Hischier concluded that the P_1 approximation was the most accurate approach. The Rosseland approximation led to inaccurate results due to the relatively small optical thickness. Doermann and Sacadura [41] applied the Rosseland diffusion approximation successfully to evaluate radiative heat transfer for 10 ppi carbon foam with an optical thickness of ~13.

Chapter 3

Design and modeling of the heat exchanger

3.1 Design

The design of the counterflow reticulate porous ceramic (RPC) heat exchanger is constrained by the methods available to integrate the heat exchanger with the reactor and operating temperatures up to 1773 K as introduced in chapter 1. As discussed in chapter 2, the use of superalloys are limited to 1123 K due to a significant decline in their thermo-mechanical properties [5] which limits the materials of construction to ceramics such as alumina (Al_2O_3) and silicon carbide (SiC). Gas tight seals are also required at the interface of the reactor cavity and the heat exchanger which necessitates ceramic-ceramic bonding at 1773 K. In light of these constraints, an alumina tube-in-tube heat exchanger (HX) is proposed as shown schematically in figure 3.1. The heat exchanger is an extension of the reactive element and is integrated with the element by means of a shrink-fit joint with an alumina collar. The radii of the inner and outer tubes are fixed to match the radii of the tubes in the reactive element for ease of integration with the shrink-fit collar joint at 1773 K. (The effect of varying the radial dimensions on the HX performance is analyzed in Appendix A). The inner tube has an inner diameter (i.d.), D_1, of 38.1 mm and outer diameter (o.d.), D_2, of 44.4 mm whilst the outer tube has an i.d., D_3, of 63.6 mm, and o.d. of 69.9 mm. Both tubes are constructed of the same purity dense alumina as used in the reactive element to match the coefficient of thermal expansion. The tube and the annular region are filled with alumina reticulate porous ceramic (RPC) to significantly boost the surface area for heat transfer between the hot and cold gas streams. SiC despite its higher bulk solid thermal conductivity is not selected as it is

actively oxidizes at temperatures above 1673 K and poses challenges in high temperature gas connections (explained in greater detail in Appendix B). Alumina does not share these problems and is therefore selected as the RPC material.

To specify the design of the heat exchanger, the length of the heat exchanger (L) and the RPC morphology i.e. porosity and pore density are selected based on the results of a fluid flow and heat transfer analysis of the heat exchanger.

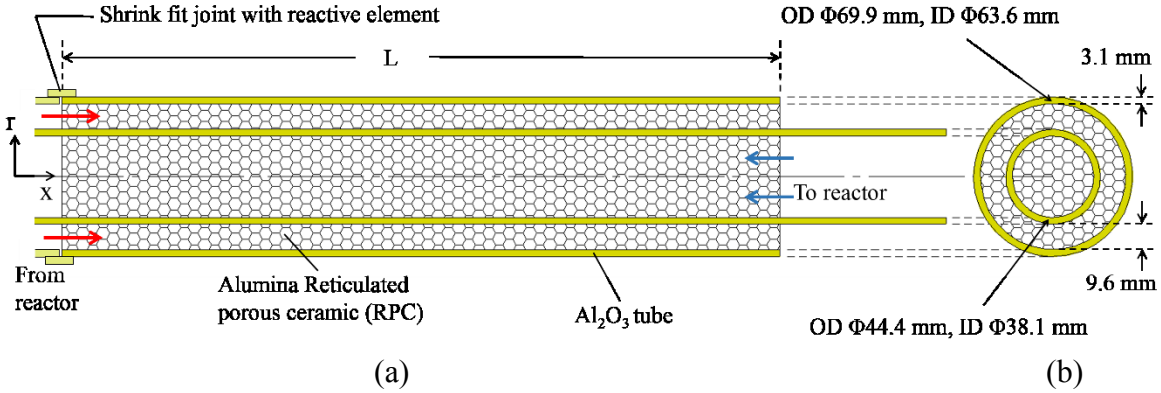

Figure 3.1 (a) Cross-section and (b) front section view of a single counterflow alumina RPC filled tube-in-tube heat exchanger. The figure is not to scale.

3.2 Modeling

3.2.1 Overview

The heat exchanger was specified using a two-step modeling approach. In the first modeling step, the effect of porosity and pore density of the alumina RPC on the fluid flow and heat transfer performance of the heat exchanger as a function of gas flow rate was analyzed. The non-dimensional volume-averaged equations of mass and momentum for hydraulically fully developed forced convective flow through the RPC-filled tube and annulus of the heat exchanger were solved to obtain dimensionless velocity profiles. The dimensionless temperature profiles were obtained using the analytical solution to the volume-averaged energy equation derived by Lu and Zhao et al. [12, 13]. The computed

profiles are used to calculate the overall heat transfer coefficient, U_t, and pressure drop per unit length, $\Delta p/L$, which are used to quantify the hydraulic and thermal performance. For a given set of flow rates ($\dot{n}_c$ and $\dot{n}_h$) and hot and cold inlet temperatures ($T_{h,i}$ and $T_{c,i}$), a higher U_t leads to higher heat transfer between the hot and cold stream and consequently, higher heat exchanger effectiveness,

$$\epsilon = \frac{\dot{n}_c\left(\bar{H}_c(T_{c,o}) - \bar{H}_c(T_{c,i})\right)}{\dot{n}\left(\bar{H}(T_{h,i}) - \bar{H}(T_{c,i})\right)\Big|_{min}} = \frac{\dot{n}_h\left(\bar{H}_h(T_{h,i}) - \bar{H}_h(T_{h,o})\right)}{\dot{n}\left(\bar{H}(T_{h,i}) - \bar{H}(T_{c,i})\right)\Big|_{min}} = \frac{U_t A_t (T_h - T_c)}{\dot{n}\left(\bar{H}(T_{h,i}) - \bar{H}(T_{c,i})\right)\Big|_{min}} \quad (3.1)$$

Therefore, the chosen combination of RPC material, porosity and pore density should maximize U_t (>150 W m^{-2} K^{-1}) and provide an acceptable value of $\Delta p/L$ (<2×10^4 Pa m^{-1}). The input parameters for the analysis are listed in Table 3.1. The chosen gas flow rate of 6.4×10^{-2}mol s^{-1} is representative of the flow rates expected during reduction (5×10^{-2}mol s^{-1} to 8.9×10^{-2}mol s^{-1}) for CO_2 splitting. At pore densities below 10 ppi, the volume-averaging approach to solving the transport equations in the annulus breaks down since the annular gap (domain length) is of the same order of magnitude as the pore diameter. Therefore, pore densities below 10 ppi are not modeled in this study.

Table 3.1 Baseline values and ranges studied for first modeling step

Input	Baseline	Parametric range
R_1	19.1 mm	-
R_2	22.2 mm	-
R_3	31.8 mm	-
$\dot{n}$	6.4×10^{-2} mol s^{-1}	-
ϕ	0.85	0.7, 0.75, 0.8, 0.85, 0.9
ppi	10	10, 20, 30
k_s[1]	30 – 5.6 W m^{-1} K^{-1} (Alumina)	-
k_f[1]	0.03 – 0.12 W m^{-1} K^{-1} (Nitrogen)	-

[1]over the temperature range 298 – 1773 K

With the porosity and pore density of the alumina RPC selected, the length of the heat exchanger is specified based on the results of a 1-D radially lumped, numerical model in the second modeling step. The numerical model evaluates the gas outlet temperatures, heat exchanger effectiveness, ϵ, and pressure drop across the heat exchanger, Δp, for a given length, L, gas flow rate, $\dot{n}$ and gas inlet temperatures. The hot and cold gas inlet temperatures are fixed at 1773 K and 298 K respectively. The gas flow rate is specified by an energy balance on the solar thermochemical reactor as described by Venstrom et al. [2]. In the energy balance, one of the inputs is the temperature of the gas entering the reactor which is equivalent to the gas temperature at the cold outlet of the heat exchanger downstream. The gas temperature at the cold outlet, $T_{c,o}$, is obtained from the numerical model. Consequently, the energy balance (input: $T_{c,o}$; output: $\dot{n}$) and the numerical model (input: $\dot{n}$; output: $T_{c,o}$) are coupled and need to be solved iteratively to obtain converged values of $\dot{n}$ and $T_{c,o}$ for a specified L. The energy balance is given in eq (3.2),

$$q_{\text{solar}} = \frac{\sigma T_{\text{R}}^4}{CI} q_{\text{solar}} + F_L q_{\text{solar}} \left(1 - \frac{\sigma T_{\text{R}}^4}{CI}\right) + \bar{\dot{n}}'_{\text{f}} \times \Delta H_{\text{r}}|_{T_{\text{R}}} + \left(\frac{\tau_{rd}}{\tau_{rd} + \tau_{ox}}\right) \dot{n}'_{sg} \left[\bar{H}_{\text{sg}}(T_{\text{R}}) - \bar{H}_{\text{sg}}(T_{\text{sg,c,o}})\right] + \left(\frac{\tau_{ox}}{\tau_{rd} + \tau_{ox}}\right) \dot{n}'_{ox} \left[\bar{H}_{\text{ox}}(T_{\text{R}}) - \bar{H}_{\text{ox}}(T_{\text{ox,c,o}})\right] \tag{3.2}$$

The term on the left hand side represents the solar input per unit mass of ceria. The first term on the right hand side accounts for the energy lost to reradiation assuming a blackbody cavity receiver and a concentration ratio (C) of 3000 at the cavity aperture. The second term accounts for the energy lost due to convection and conduction through

the reactor insulation as afraction of the absorbed solar input (F_L). Based on a thermal analysis of the reactor insulation, F_L is fixed at 0.32. The third term is the energy sink associated with the fuel production reaction where $\bar{\dot{n}}'_{\mathrm{f}}$ is the average rate of fuel produced per unit mass of ceria and $\Delta H_{\mathrm{r}}|_{T_{\mathrm{R}}}$is the reaction enthalpy evaluated at the reactor temperature, T_{R} fixed at 1773 K. The last two terms on the right hand side account for the sensible heat required to raise the temperatures of the sweep gas and oxidizer streams from the cold outlet of the heat exchanger, $T_{\mathrm{sg,c,o}}$ and $T_{\mathrm{ox,c,o}}$, to T_{R}. The ceria mass specific sweep gas and oxidizer flow rates, $\dot{n}'_{sg}$ and $\dot{n}'_{ox}$, are fixed at 1×10^{-4}mols^{-1} g^{-1} and 3.4×10^{-5}mol s^{-1} g^{-1} for CO_2 splitting. The durations of reduction, τ_{rd}, and oxidation, τ_{ox}, are 100 s. The flow rates and durations are selected to maximize reactor efficiency based on experimental studies performed by Venstrom et al. [2]. $T_{\mathrm{sg,c,o}}$ and $T_{\mathrm{ox,c,o}}$ are evaluated by the 1-D numerical model. After evaluating q_{solar}, the ceria mass in the reactor is calculated as,

$$m_{ceria} = \frac{\dot{Q}_i}{q_{solar}} \tag{3.3}$$

where, the solar input to the reactor, $\dot{Q}_i$, is fixed at 3 kW. The gas flow rates required as inputs to the numerical model, $\dot{n}_{sg}$and $\dot{n}_{ox}$, are subsequently obtained by scaling the ceria mass specific flow rates with m_{ceria}. The values of the input parameters to the energy balance are listed in Table 3.2.

The reactor efficiency,η, is used as the performance metric to specify L,

$$\eta = \frac{\bar{\dot{n}}'_{\mathrm{f}} * HHV_{\mathrm{f}}}{q_{solar} + p_{pump}} \tag{3.4}$$

The pumping power per unit mass of ceria required to drive the gas flow through the heat exchanger, p_{pump}, is defined as

$$p_{pump} = \frac{1}{m_{ceria}} \frac{1}{\eta_{pump}} \frac{\gamma}{\gamma - 1} \dot{n} R T_i \left(\left(\frac{p_o}{p_i} \right)^{\frac{\gamma - 1}{\gamma}} - 1 \right) \tag{3.5}$$

where, η_{pump} is the isentropic pumping efficiency, γ is the ratio of the specific heat at constant pressure to the specific heat at constant volume for the gas, R is the universal gas constant, T_i is the gas inlet temperature to the pump, p_i is the gas pressure at the pump inlet and p_o is the pressure at the pump outlet,

$$p_o = p_i + \Delta p \tag{3.6}$$

Table 3.2 Input parameters for the reactor energy balance

Input	Value
T_R	1773 K
σ	5.67×10^{-8} W m^{-2} K^{-4}
C	3000
I	1000 W m^{-2}
F_L	0.32
$\bar{\dot{n}}'_{\mathrm{f}}$	7.8×10^{-8} mol s^{-1} g^{-1}
$\dot{n}'^{\,3}_{sg}$	1×10^{-4} mol s^{-1} g^{-1}
$\dot{n}'^{\,3}_{ox}$	3.4×10^{-5} mol s^{-1} g^{-1}
τ_{rd}	100 s
τ_{ox}	100 s
T_{i}	298 K
$\dot{Q}_{in}$	3000 W
HHV_{f}^{2}	2.8×10^{5} J mol^{-1}
η_{pump}	0.8
γ	1.4 (sweep gas) 1.28 (oxidizer)
R	8.314 J mol^{-1} K^{-1}
L	1.4 m

[1]over the temperature range 298 – 1773 K

[2]for CO

[3]evaluated at T=298 K and P=1 bar

The coupled reactor energy balance and numerical model are solved for a range of heat exchanger lengths, 0.05≤ L≤1.6 m. The selected heat exchanger length maximizes η.

3.2.2 The overall heat transfer coefficient

The overall heat transfer coefficient based on the inner surface area of the tube, U_t, along with the pressure drop per unit length in the annulus, $\frac{\Delta p_{an}}{\mathrm{L}}$, and the tube, $\frac{\Delta p_t}{\mathrm{L}}$, are obtained by solving the non-dimensional steady-state volume averaged mass and momentum transport equations for fluid flow through porous media and using the analytical solution for the energy transport equation derived by Lu and Zhao et al [12, 13].

To obtain a solution of the non-dimensional mass and momentum equations, the flow is assumed to be hydraulically and thermally fully developed i.e. $\frac{\partial \vec{V}}{\partial x} = 0$ and $\frac{\partial T_f}{\partial x} = \frac{\partial T_s}{\partial x} = \frac{\partial T_w}{\partial x} = constant$, the porous medium is assumed to be homogeneous and isotropic and all thermophysical properties of the solid and fluid are assumed to be independent of temperature. Based on these assumptions, on introducing the non-dimensional variables, $D = \frac{K}{R_1^2}$, $\psi = \frac{r}{R_1}$, $U = \frac{u}{\bar{u}_t}$, $P = \frac{\left(\frac{dp}{dx}\right)}{\left(\frac{\mu_f \bar{u}_t}{K} + \rho_f F \bar{u}_t^2\right)}$, $Re_{D_1} = \frac{\rho_f \bar{u}_t 2R_1}{\mu_f}$, $C_F = \frac{FR_1}{2}$, the mass and momentum equations are given by eqs (3.7) and (3.8),

$$\frac{1}{A}\int UdA = 1 \tag{3.7}$$

$$0 = -P\left(\frac{1}{D} + Re_{D_1} C_F\right) + \frac{1}{\phi\psi}\frac{\partial}{\partial\psi}\left(\psi\frac{\partial U}{\partial\psi}\right) - \frac{\mathrm{U}}{\mathrm{D}} - Re_{D_1} C_F U^2 \tag{3.8}$$

for the tube. For the annulus, the characteristic length scale, R_1 is replaced by the outer radius of the inner tube, R_2. The dimensionless pressure drop, P and the dimensionless

radial velocity, U are obtained by solving eq (3.7) and eq (3.8) simultaneously using the finite volume technique outlined by Patankar [43]. Figure 3.2 shows a sketch of the modeling domain along with the prescribed boundary conditions. The modeling domain is discretized radially into 'm' finite volumes with nodes placed in the middle of each volume. Two additional nodes are placed at the boundaries of the domain. The nodal velocities are solved iteratively and converge when the condition $\sqrt{\sum_{p=1}^{m+2}\left(\frac{u_p^{k+1}-u_p^k}{u_p^k}\right)^2} < 10^{-6}$ is satisfied for two consecutive iteration steps k and k+1.

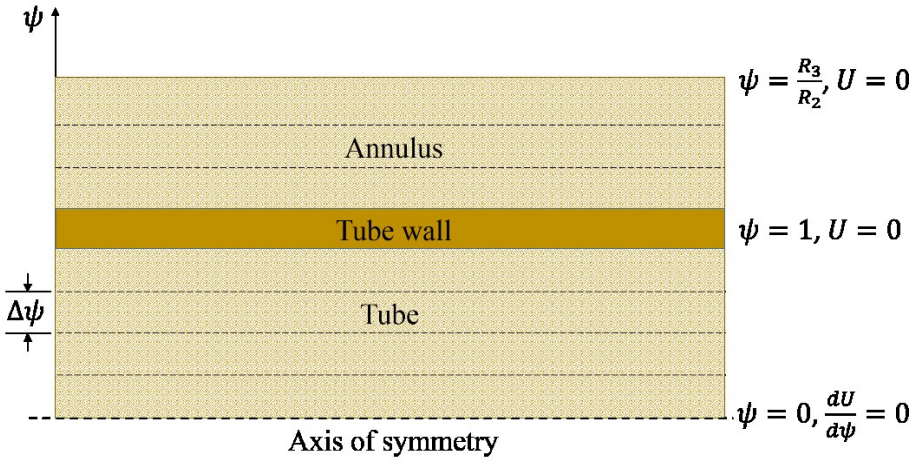

Figure 3.2 Modeling domain with boundary conditions for the numerical solution of the dimensionless mass and momentum equations.

The non-dimensional energy equations for the solid and fluid phases have been solved analytically by Lu et al. [12] and Zhao et al. [13] respectively, to obtain the dimensionless solid phase (θ_s) and fluid phase (θ_f) radial temperature distributions used here. To obtain an analytical solution, Lu and Zhao make a series of simplifying assumptions in addition to the assumptions made for the numerical solution to the mass and momentum equations:

- The outer wall of the outer tube is perfectly insulated.

- A uniform heat flux is applied on the inner tube wall boundary.
- The effect of thermal dispersion and natural convection is negligible.
- There is no axial conduction along the tube wall and radial conduction in the wall is modeled assuming a logarithmic temperature distribution.
- Radiation heat transfer in the solid phase is modeled using the Rosseland diffusion approximation which defines a 'radiative' conductivity,

$$k_{rad} = \frac{16\sigma T_s^3}{3\beta} \tag{3.9}$$

The assumption of an adiabatic outer tube is unrealistic. Applying the Rosseland diffusion approximation even though the optical thickness of the annular foam, defined as the product of the extinction coefficient (β) and the annular gap, is <10 for 10 ppi foam can overestimate the radiative source term as discussed in the earlier chapter and shown in [40]. Axial conduction in the tube walls is neglected and conduction in the radial direction is modeled using a simplified analytical expression which precludes a reliable stress analysis of the tubes. These limitations are absent in a more sophisticated 2-D axisymmetric finite element model of the heat exchanger developed by Bala Chandran [42].

Based on these simplifying assumptions, on introducing the dimensionless variables, $B = \frac{h_{sf}\tilde{a}R_1^2}{k_{se}}$, $\psi = \frac{r}{R_1}$, $U = \frac{u}{\bar{u}_t}$, $A = \frac{k_{fe}}{k_{se}+k_{rad}}$, $\theta = \frac{T-T_w}{q_w R/k_{se}}$, the non-dimensional energy equation for the solid phase is given by

$$B\left(\theta_s - \theta_f\right) = \frac{\partial^2\theta_s}{\partial\psi^2} + \frac{1}{\psi}\frac{\partial\theta_s}{\partial\psi} \tag{3.10}$$

and for the fluid phase is given by

$$2U = A\left(\frac{\partial^2\theta_f}{\partial\psi^2} + \frac{1}{\psi}\frac{\partial\theta_f}{\partial\psi}\right) + B\left(\theta_s - \theta_f\right) \tag{3.11}$$

Eqs (3.10) and (3.11) are Bessel differential equations in θ_s and θ_f whose canonical solutions are modified Bessel functions of the 1st and 2nd kind.

The effective fluid flow and thermal transport properties of the porous medium are estimated from existing correlations developed for open cell foams. Table 3.3 summarizes the various correlations used to evaluate the properties and cites their sources. As mentioned in the previous chapter, although most of the correlations are based on experimental data for open cell metal foams, they have been found to correlate well with data obtained for RPCs [22, 23, 57]. Metal and ceramic open cell foams manufactured using the sintering technique have similar features including dodecahedral unit cells and triangular hollow struts. As the effective transport properties primarily depend on foam morphology, a good correlation can be obtained between metal and ceramic foams.

With the dimensionless pressure drop, velocity and temperature profiles known, the overall heat transfer coefficient and axial pressure gradients can be calculated. The overall heat transfer coefficient based on the inner surface area of the tube is given by

$$U_t = \frac{1}{\left(\frac{1}{\bar{h}_t} + \frac{R_1 ln(R_2/R_1)}{k_w} + \frac{R_1}{R_2\bar{h}_{an}}\right)} \tag{3.12}$$

The average heat transfer coefficient averaged over the inner surface area of the tube is given by

$$\bar{h}_t = -\frac{k_{se}}{\bar{\theta}_{f_t} R_1} \tag{3.13}$$

Table 3.3 Determination of effective transport properties of RPCs

Property	Correlations for open cellular foams	Source
d_p	$d_p = \frac{0.0254}{ppi}$ m	[32]
d_{st}	$d_{st} = 1.18 d_p \sqrt{\frac{1-\phi}{3\pi}} \left(1 - e^{-\left({}^{(1-\phi)}/_{0.04}\right)}\right)^{-1}$ m	[32]
$\tilde{a}$	$\tilde{a} = \frac{3\pi d_{st}\left(1 - e^{-\left({}^{(1-\phi)}/_{0.04}\right)}\right)}{\left(0.59 d_p\right)^2}$ $\mathrm{m^{-1}}$	[32]
K	$K = \frac{\phi^3}{k_K \tilde{a}^2}$ $\mathrm{m^2}$	[22, 32]
F	$F = \frac{0.3\tilde{a}}{\phi^3}$ $\mathrm{m^{-1}}$	[22, 32]
h_{sf}	$h_{sf} = \frac{k_f}{d_p}\left(1.559 + 0.5954 Re_{d_p}^{0.5626} Pr^{0.472}\right)$ $\mathrm{Wm^{-2}K^{-1}}$; $0.2 < Re_{d_p} < 200$	[20, 22]
k_{se}	$k_{se} = \frac{0.8(1-\phi)k_s}{3}$ $\mathrm{Wm^{-1}K^{-1}}$	[16, 28, 29]
k_{fe}	$k_{fe} = \phi k_f$ $\mathrm{Wm^{-1}K^{-1}}$	[16, 28, 29]
β	$\beta = \frac{4.4}{d_p}(1-\phi)$ $\mathrm{m^{-1}}$	[35, 36, 37]

where, $\bar{\theta}_{f_t}$ is the dimensionless bulk-mean fluid temperature in the tube and is calculated by

$$\bar{\theta}_{f_t} = 2\int_0^1 U\theta_f \psi d\psi \tag{3.14}$$

The heat transfer coefficient averaged over the annulus is given by

$$\bar{h}_{an} = -\frac{k_{se}}{\bar{\theta}_{f_{an}} R_2} \tag{3.15}$$

where, $\bar{\theta}_{f_{an}}$ is the dimensionless bulk-mean fluid temperature in the annulus and is calculated by

$$\bar{\theta}_{f_{an}} = 2\int_1^{\frac{R_3}{R_2}} U\theta_f \psi d\psi \tag{3.16}$$

The axial pressure gradient in the inner tube is given by

$$\frac{\Delta p_t}{\mathrm{L}} = \left(\frac{\mu_f \bar{u}_t}{K} + \rho_f F \bar{u}_t^2\right) P_t \tag{3.17}$$

The axial pressure gradient in the annulus is given by

$$\frac{\Delta p_{an}}{\mathrm{L}} = \left(\frac{\mu_f \bar{u}_{an}}{K} + \rho_f F \bar{u}_{an}^2\right) P_{an} \tag{3.18}$$

3.2.3 Numerical model

A 1-D, radially lumped, numerical model was developed to determine the effectiveness, ϵ, and the total pressure drop across the heat exchanger (Δp) as a function of the gas flow rate, $\dot{n}$, and the heat exchanger length, L. Due to the difference in gas flow rate and composition during reduction and oxidation, the heat exchanger is sized for the higher thermal capacitance flow which for the case of CO_2 splitting is the reduction sweep gas flow. To capture the temperature-dependent thermophysical properties of the gas and the temperature-dependent effective transport properties of the RPC, the hot and cold sides of the HX were discretized into 'n' finite volume elements of length 'Δx'. Each finite volume element is a heat exchanger whose inlet conditions are the outlet conditions of the element preceding it.

The outlet temperature of a finite volume element 'j' is obtained from an energy balance given by eq (3.19) and shown schematically in figure 3.3,

$$\dot{n}_h c_{p,h}(T_{h,i})\Delta T_h\big|_j = \dot{n}_c c_{p,c}(T_{c,i})\Delta T_c\big|_j = \dot{Q}_j \tag{3.19}$$

Therefore,

$$T_{h,o}\big|_j = T_{h,i}\big|_j - \frac{\dot{Q}_j}{\dot{n}_h c_{p,h}(T_{h,i})\big|_j} \tag{3.20}$$

for the hot stream, and,

$$T_{c,o}\big|_j = T_{c,i}\big|_j + \frac{\dot{Q}_j}{\dot{n}_c c_{p,c}(T_{c,i})\big|_j} \tag{3.21}$$

for the cold stream. The heat transferred from the hot stream to the cold stream in the element 'j', is given by

$$\dot{Q}_j = 2\pi R_1 \Delta x U_{t,j} \Delta T_j \tag{3.22}$$

where ΔT_j is the temperature difference between the hot and cold streams for each element 'j',

$$\Delta T_j = T_{h,i}\big|_j - T_{c,i}\big|_j \tag{3.23}$$

The overall heat transfer coefficient based on the inner surface area of the tube for the element 'j', $U_{t,j}$, is obtained using eq (3.12) described in section 3.2.2.

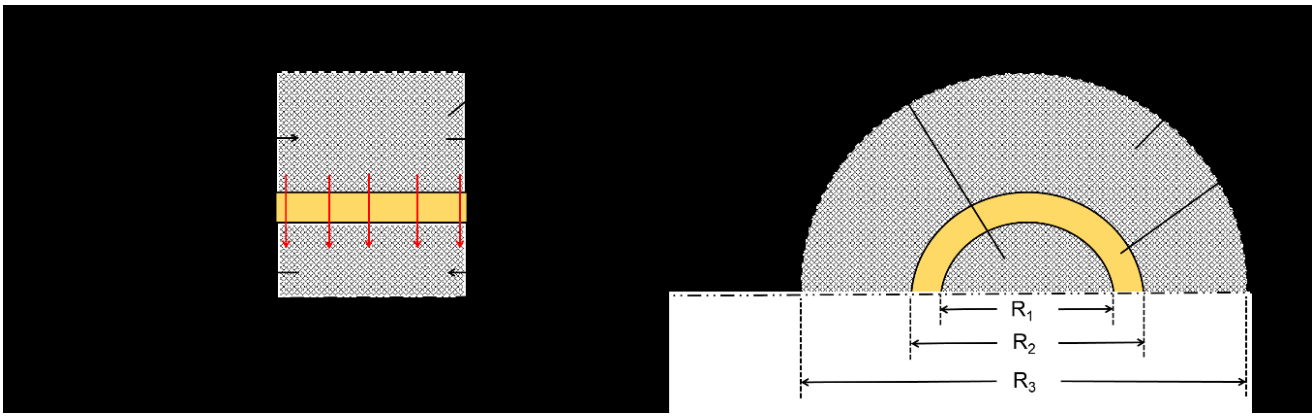

Figure 3.3 Energy flows in a finite volume element 'j' of the HX.

The pressure at the outlet of element 'j' is obtained using eq (3.24) for the tube and eq (3.25) for the annulus,

$$p_{t,o}\big|_j = p_{t,i}\big|_j + \frac{\Delta p_t}{\Delta x}\Big|_j \Delta x \tag{3.24}$$

$$p_{an,o}\big|_j = p_{an,i}\big|_j + \frac{\Delta p_{an}}{\Delta x}\Big|_j \Delta x \tag{3.25}$$

To evaluate the temperature and pressure profiles in the heat exchanger, the overall heat transfer coefficient, $U_{t,j}$, and the axial pressure gradients, $\frac{\Delta p_t}{\Delta x}\Big|_j$ and $\frac{\Delta p_{an}}{\Delta x}\Big|_j$ for

element ‘j’ are calculated by solving the volume averaged mass, momentum and energy equations for porous media as described in section 3.2.2. These parameters depend on the local thermophysical properties of the gas and the local temperature dependent transport properties of the RPC. Thus, an iterative solution for the temperature profile is required. The solution is said to have converged when the condition $\sqrt{\sum_{j=1}^{n}\left(\frac{T_j^{k+1}-T_j^k}{T_j^k}\right)^2} < 10^{-6}$ is satisfied for two consecutive iteration steps k and k+1.

Once the temperature profiles on the hot and cold sides of the heat exchanger have converged, the total heat transfer in the heat exchanger is calculated using eq (3.26) and the total pressure drop across the heat exchanger is calculated using eq (3.27),

$$\dot{Q} = \sum_{j=1}^{n} 2\pi R_1 \Delta x U_{t,j} \Delta T_j \tag{3.26}$$

$$\Delta p = \sum_{j=1}^{n} \Delta p_{an}|_j + \sum_{j=1}^{n} \Delta p_t|_j \tag{3.27}$$

Finally, the effectiveness of the heat exchanger is given by eq (3.1).

3.2.4 Results and Discussion

3.2.4.1 Selecting RPC morphology and composition

Figure 3.4 shows the variation of the overall heat transfer coefficient with foam morphology namely, porosity and pore density, for alumina RPC. From the figure, it can be seen that as porosity (φ) increases from 0.7 to 0.9, U_t decreases from 166 to 152 W m^{-2} K^{-1} for 10 ppi foam despite a decrease in the extinction coefficient (Table 3.3) which in turn, increases the radiative conductivity, eq (3.9). Similar trends are observed for all pore densities considered. The decrease in U_t with increase in φ is attributed to a decrease

in the solid volume fraction of the porous media which reduces the effective solid phase thermal conductivity of the media. The results show that for the range of porosities studied, the effect of heat diffusion due to pure conduction through the solid phase outweighs the effect of radiation. Increasing the pore density from 10 to 30 ppi leads to a decrease in U_t for the range of porosities considered despite increasing the specific surface area available for heat transfer from the solid to the fluid phase in the media from 1590 m^{-1} to 4760 m^{-1}. Increasing the pore density from 10 to 30 ppi increases the extinction coefficient by an order of magnitude, 416 to 1247 m^{-1} for φ=0.85. As the extinction coefficient increases, radiation is attenuated. Consequently, U decreases from 153 to 104 W m^{-2} K^{-1} for φ=0.85. Similar trends are observed for all porosities considered. The results show that for the range of pore densities studied, radiation dominates over convection.

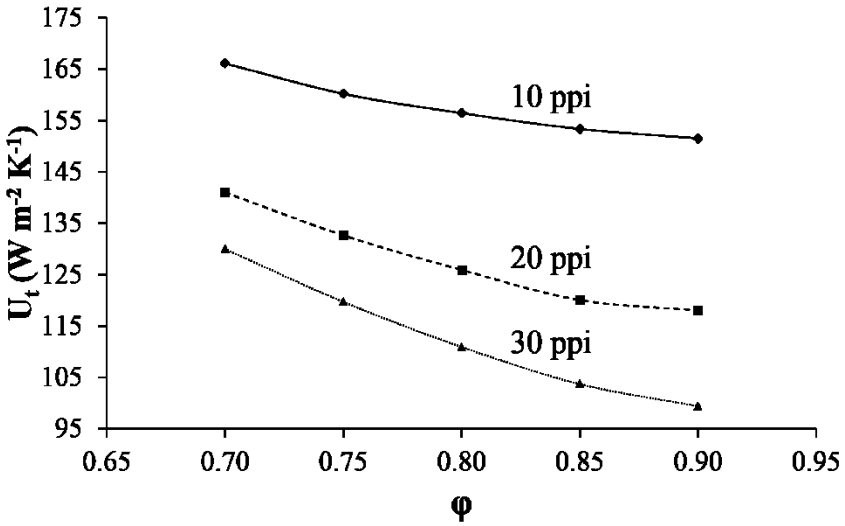

Figure 3.4 Variation of overall heat transfer coefficient with foam morphology.

Figure 3.5 shows the variation of the pressure drop across the heat exchanger with porosity and pore density for alumina RPC. As expected, the pressure drop increases with an increase in the solid volume fraction and pore density of the media due to increased

pore-level viscous drag and form drag forces. For φ=0.85, the pressure drop increases from 1.3×10^4 to 6.6×10^4 Pa m^{-1} as the pore density increases from 10 to 30 ppi. Similar trends are observed for all porosities considered. The pressure drop across the heat exchanger affects the pressure in the ceria bed preceding it in the reactor and consequently the ceria thermodynamics (as discussed in greater detail in Appendix C). Assuming the partial pressure of oxygen in the ceria bed is constant and is equal to the partial pressure of oxygen at the bed inlet, for an oxygen concentration of 10 ppm during reduction, the equilibrium fuel production is estimated to decrease by 16% relative to the fuel produced with a ceria bed pressure of 1×10^5 Pa during oxidation for a 70% porous, 10 ppi foam. Increasing the porosity to 90% reduces the pressure in the bed significantly. Therefore, the equilibrium fuel produced is estimated to decrease only marginally by 2.5% relative to the base case of 1×10^5 Pa pressure in the ceria bed.

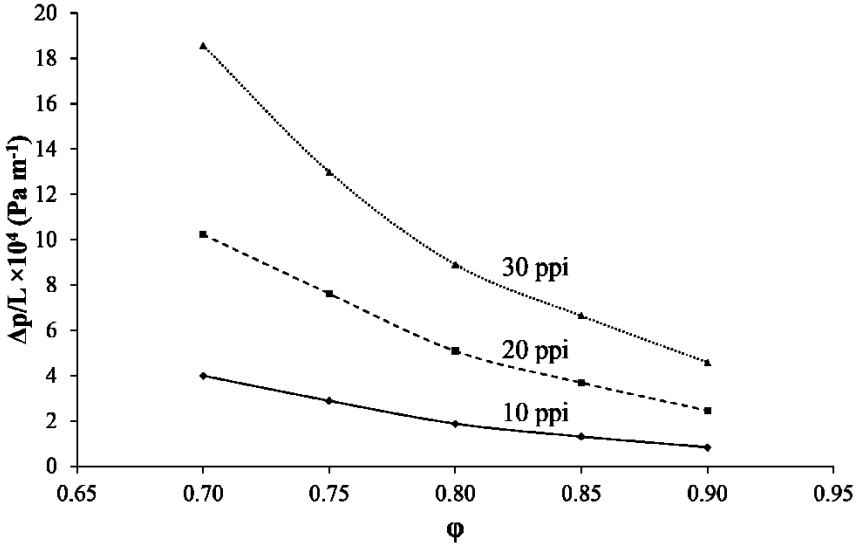

Figure 3.5 Variation of pressure drop across the heat exchanger with foam morphology.

Based on these results, a porosity of 85% and pore density of 10 ppi is selected as it significantly enhances the heat transfer in the media (>150 W m^{-2}) and provides

acceptable pressure drop (<2×10^4 Pa m^{-1}), reducing the equilibrium fuel production by a marginal 4% relative to the base case.

3.2.4.2 Selecting the heat exchanger length

Figure 3.6 is a plot of the heat exchanger effectiveness as a function of L. The effectiveness as expected increases asymptotically with length and is almost flat beyond a length of 0.8 m with a marginal 4.4% and 2.5% relative increase in reduction and oxidation heat exchanger effectiveness when increasing the length from 0.8 to 1.6 m.

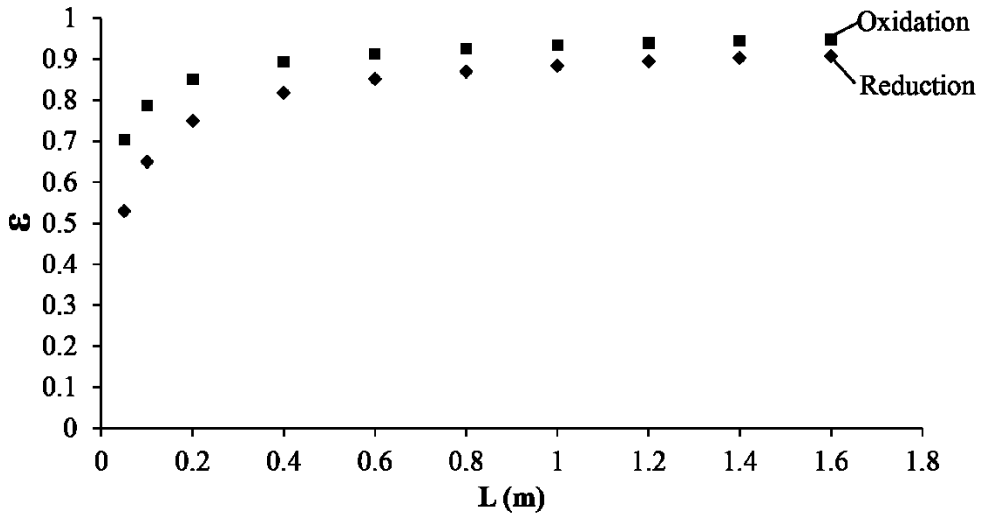

Figure 3.6 Variation of reduction and oxidation heat exchanger effectiveness with length for 85% porous, 10 ppi alumina RPC.

Figure 3.7 shows the variation of the reactor efficiency with heat exchanger length. The efficiency initially increases from 0.8% to a peak of 2.8% as the length increases from 0.05 to 1.4 m before starting to decrease at L=1.6 m. The relative percent increase in η decreases from 27.8% when increasing the length from 0.1 to 0.2 m to 0.4% when increasing the length from 1.2 to 1.4 m. The decrease in the relative percent increase in η shows the diminishing returns with increases in L. To maximize η, the length of 1.4 m which corresponds to the peak efficiency is selected. The complete design

specifications of the heat exchanger for reduction and oxidation for CO_2 splitting are listed in Table 3.4.

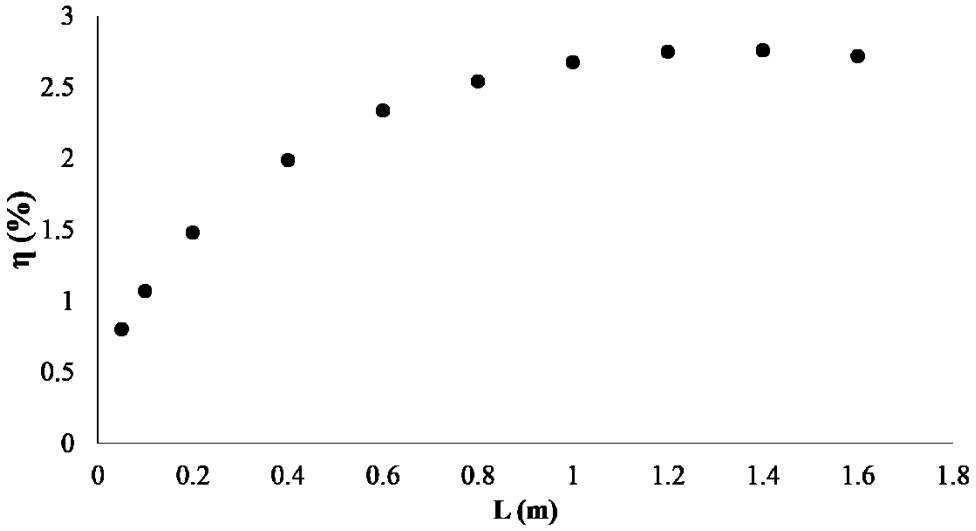

Figure 3.7 Variation of reactor efficiency with heat exchanger length for 85% porous, 10 ppi alumina RPC.

Table 3.4 Heat exchanger design specifications

Design Parameter	Value
Inner tube inner radius	19.1 mm
Inner tube outer radius	22.2 mm
Outer tube inner radius	31.8 mm
Outer tube outer radius	34.9 mm
Length	1.4 m
Sweep gas flow rate (N_2)	8.5×10^{-2} mol s^{-1}
Effectiveness of heat recovery (reduction)	90.3%
Pressure drop across heat exchanger (reduction)	2.8×10^{4} Pa
Heat transfer duty (reduction)	3731 W
Oxidizer flow rate (CO_2)	2.8×10^{-2} mol s^{-1}
Effectiveness of heat recovery (oxidation)	94.5%
Pressure drop across heat exchanger (oxidation)	6×10^{3} Pa
Heat transfer duty (oxidation)	2044 W

3.2.4.3 Comparison with 2-D CFD model

As explained in section 3.2.2, the 1-D numerical model makes a number of simplifying assumptions which are overcome by a more sophisticated 2-D axisymmetric finite element model of the heat exchanger developed by Bala Chandran [42].

Figures 3.8 and 3.9 compare the performance predicted by the 1-D model and 2-D models for a 1.4 m long, 10 ppi alumina RPC filled heat exchanger. The 1-D model overestimates the radiative source term as defined in eq (3.9) at higher porosities. Consequently, the difference in the predicted effectiveness between the two models increases from 0.6% to 1% relative to the effectiveness predicted by the 1-D model as the porosity increases from 0.8 to 0.9. The pressure drop variations between the two models can be attributed to the differences in the temperature dependent thermophysical and effective transport properties of the porous media in the two models due to a variation in the estimated steady state temperature distributions.

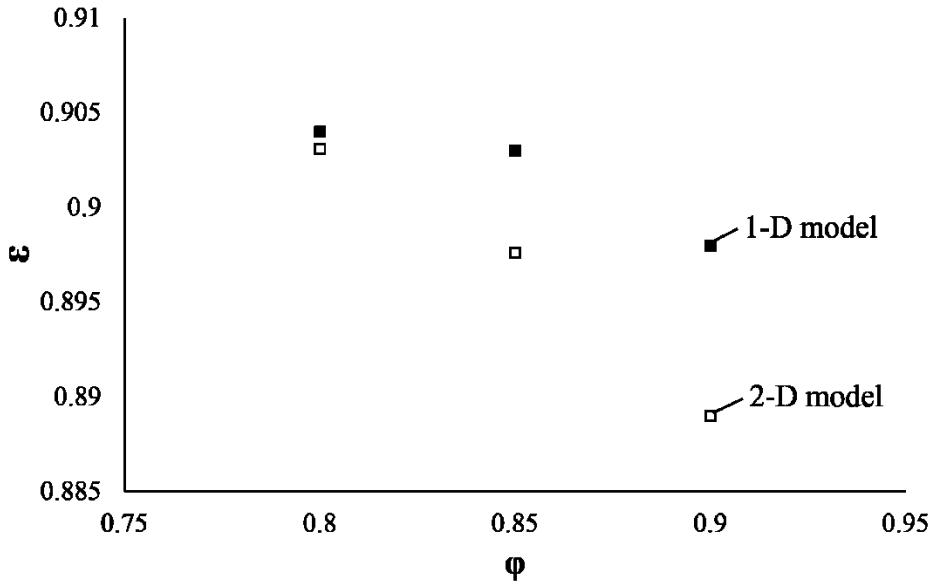

Figure 3.8 Comparison of estimated effectiveness as a function of foam porosity for a 1.4 m long, 10 ppi alumina RPC filled heat exchanger.

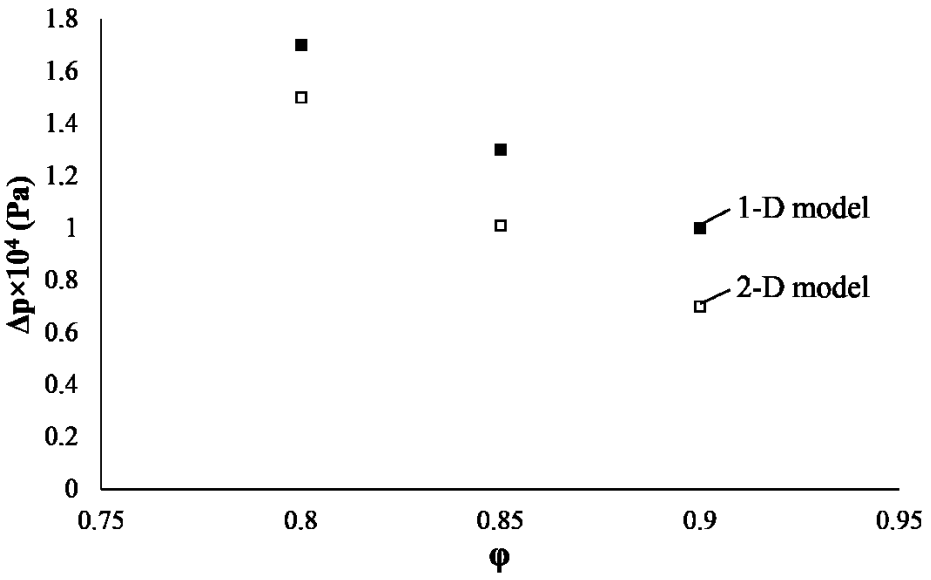

Figure 3.9 Comparison of estimated pressure drop as a function of foam porosity for a 1.4 m long, 10 ppi alumina RPC filled heat exchanger.

However, neither model takes into account the effect of contact resistance at the interface of the tube walls and the RPC and the effect of bypass flow. To analyze the impact of these effects, the hydraulic and thermal performance of a heat exchanger prototype is evaluated experimentally.

Chapter 4

Experimental investigation of alumina reticulate porous ceramic heat exchanger for high temperatures

The performance of a prototype alumina heat exchanger filled with reticulated porous alumina which was designed to recover sensible heat from inert and reactive gases flowing through a high temperature solar reactor for splitting CO_2 was measured at 600 K and 1240 K. The heat exchanger comprises of two concentric alumina tubes. The outer tube has an i.d. of 66.6 mm and an o.d. of 71.2 mm and the inner tube has an i.d. of 38 mm and an o.d. of 46 mm. The length of the heat exchanger is 0.4 m. The alumina RPC has a nominal porosity of 80% and a nominal pore density of 5 pores per inch (ppi) with a surface area to volume ratio of 917 m^{-1}. Measurements include the permeability, inertial coefficient, overall heat transfer coefficient, effectiveness and pressure drop over Reynolds numbers of 453-659 in the tube and 216-422 in the annulus. The overall heat transfer coefficients were 26-32 W m^{-2} K^{-1} at 600 K and 36-41 W m^{-2} K^{-1} at 1240 K for fixed hot stream molar flow rate of 1.7×10^{-2} mol s^{-1} and cold stream molar flow rates of 1.8×10^{-2} -2.7×10^{-2} mol s^{-1} with low pressure drops up to 1023 Pa.

4.1 Introduction

High temperature heat exchangers (HTHEs), arbitrarily defined to operate above 1123 K, are key to obtaining high process efficiencies in widespread applications including gas turbines [44-45], diesel combustion systems [46] and hydrogen production from sulfuric acid decomposition [8, 47-50]. Extensive work has been carried out on the design, modeling and fabrication of HTHEs since the 1980s. Strumpf et al. [51] in 1982

fabricated one of the earliest HTHEs. Straight fins made of siliconized silicon carbide (Si-SiC) fins with a height of 9.53 mm and thickness of 1.02 mm were precision cast and diffusion bonded to a slip cast siliconized silicon carbide (Si-SiC) cylindrical solar cavity receiver. Following the work by Strumpf [51], more complicated fin geometries were investigated [47, 49-50]. Urquiza [49] developed a counterflow net-shaped off-set strip fin heat exchanger made of a Ni superalloy, Inconel 617, with molten lithium fluoride (LiF) salt and He as the two working fluids. Schmidt et al. [47] improved upon the design by replacing Inconel 617 with SiC which has superior thermal and mechanical properties at high temperatures (>1123 K).

With the advancement of manufacturing methods, more compact plate-type micro channel heat exchangers have been developed to operate up to 1473 K [5, 47-50]. Meschke and Kayser [50] describe a parallel-plate compact heat exchanger for liquid-liquid heat exchange formed by milling micro channels in a Si-SiC plate and diffusion bonding the plates to form a stack. Lewinsohn et al. [5] analyzed numerically the same heat exchanger for liquid-gas heat exchange. Knitter et al. [52] modeled and outlined the manufacturing process of a similar modular ceramic heat exchanger using injection molding, for He flow rates up to 4.9 mol s^{-1} at 1223 K. Alm et al. [53] used the method outlined by Knitter [52] to fabricate and test two 17 micro channel alumina (Al_2O_3) heat exchangers in crossflow and counterflow configurations with liquid water as the working fluid.

Open cell foams have also shown great promise as heat exchange media, especially for the cooling of electronics, with significantly higher heat transfer rates and lower pressure drop than commercial finned and shell and tube heat exchangers [6, 7, 46]

due to high specific surface area, high thermal conductivity matrix and tortuous flow paths leading to high interfacial heat transfer coefficients. Boomsma et al. [6] tested seven 40 mm long, 40 mm wide and 2 mm high aluminum foam heat exchangers using water as the working fluid. For the same set of operating conditions, the open cell foam with high specific surface area (2700 m^{-1}) reduced the thermal resistance by half as compared to commercial plate and fin heat exchangers. Fend et al. [46] developed and tested a novel dense SiC honeycomb compact heat exchanger for gas-gas heat exchange at temperatures up to 1223 K. The heat exchanger comprised of 2.17 mm wide and 0.6 mm thick square channels off-set to form a honeycomb network. Heat exchanger effectiveness of up to 0.65 was reported for a thermal duty of 1600 W with a flow rate of 0.15 mol s^{-1} of air at a hot side inlet temperature of 900 K and a cold side inlet temperature of 298 K. Overall heat transfer coefficients in the range of 30-50 W/m^2-K were measured for a specific surface area of 995 m^{-1}.

In the present experimental study, permeability, K, inertial coefficient, F, overall heat transfer coefficient, U, effectiveness, ε, and pressure drop, Δp, measurements have been made for a counterflow tube-in-tube alumina reticulate porous ceramic (RPC) heat exchanger. Along with applications in gas turbines, diesel combustion systems and hydrogen production, another potential application of the alumina RPC heat exchanger is in solar thermochemical processes. The heat exchanger is used to preheat gas entering the reactor by recovering sensible heat from the outlet gas exiting the reactor at temperatures up to 1773 K. To analyze the impact of pore blockage and bypass flow, K and F was evaluated by measuring the Δp as a function of gas flow rate, $\dot{n}$, at ambient conditions. The measured values were compared with the estimated values in the absence of pore

blockage and bypass flow. The thermal performance of the heat exchanger was quantified by measuring U and ε for Reynolds numbers in the range $453 \leq Re \leq 659$ in the tube and $216 \leq Re \leq 422$ in the annulus. Hot side flow through the tube was provided by combusting methane in air at 600 K and 1240 K for a fixed flow rate ($\dot{n}_h$) of 1.7×10^{-2} mol s^{-1}. The cold side flow through the annulus was N_2 at 300 K and was varied in the range, $1.8\times10^{-2} \leq \dot{n}_c \leq 2.7\times10^{-2}$ mol s^{-1}. Thermal resistances were estimated across the tube, annulus and wall to better understand the dominant modes of heat transfer in the heat exchanger. To illustrate the effect of RPC in enhancing heat transfer, the measured U was compared against values predicted if the tubes were empty. A volume goodness factor plot (heat transfer per unit volume v/s pumping power per unit volume) was also provided. For the same flow rates and inlet temperatures, the volume goodness factor plot can be used to directly compare the performances of different heat exchange surfaces like fins, smooth tubes, RPCs, etc [54, 55]. The reliability of the heat exchanger at elevated temperatures was illustrated by comparing the measured pressure drop attained at steady-state for each experiment to the pressure drop predicted using the values of K and F measured at room temperature before the start of the experiments.

4.2 Heat exchanger design and fabrication

The heat exchanger has a tube-in-tube geometry where concentric alumina tubes are filled with alumina RPC as shown in figure 4.1. The outer alumina tube has an i.d. of 66.6 mm (D_3) and an o.d. of 71.2 mm (D_4) and the inner alumina tube has an i.d. of 38.1 mm (D_1) and an o.d. of 46 mm (D_2). The length of the heat exchanger, L, is 0.4 m. The alumina RPC has a nominal porosity (φ) of 0.8 and a nominal pore density of 5 pores per inch (ppi). The porosity and pore density of the alumina RPC were selected based on the

results obtained by Bala Chandran [42]. Figure 4.2 are images of the end of the fabricated heat exchanger. The heat exchanger was fabricated by coating the surfaces of pre-fired alumina RPC and the inner tube with alumina slurry and then sintering the assembly at 1853 K for 2 hrs. In the annulus, closed-cell alumina felt insulation was wrapped around the RPC prior to assembly with the outer tube to prevent bypass flow.

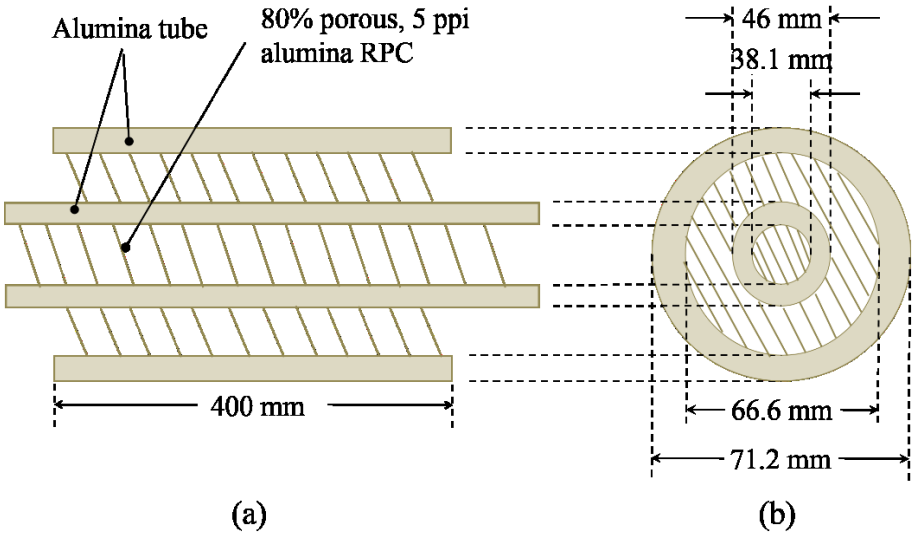

Figure 4.1 (a) Cross-section and (b) front-section view of a counterflow tube-in-tube alumina RPC filled heat exchanger. The figure is not to scale.

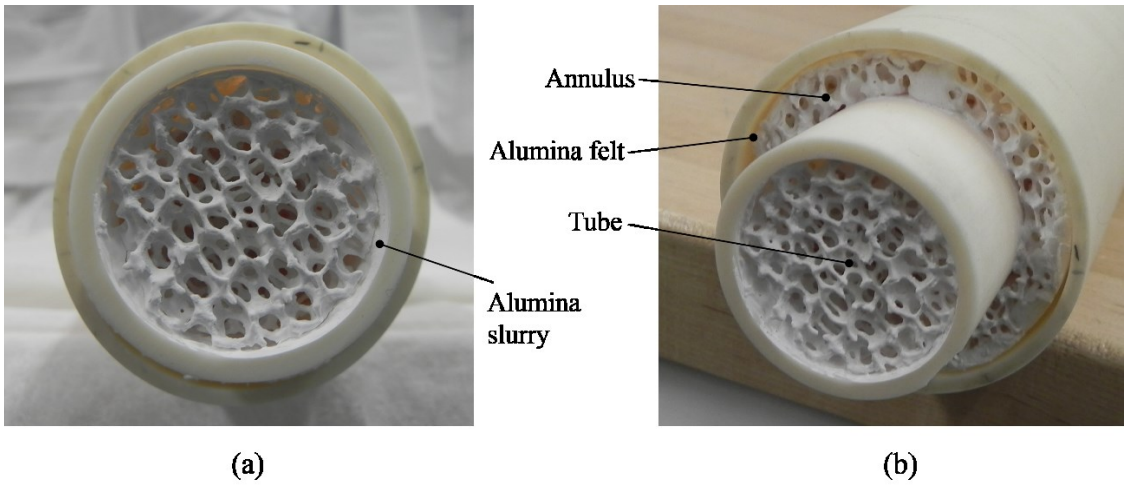

Figure 4.2 Photographic images of the end of the heat exchanger: (a) front view; (b) angled view

4.3. Experimental Methodology

4.3.1. Permeability and inertial coefficient

The schematic of the experimental apparatus used to measure pressure drop is shown in figure 4.3. Argon (Ar) at 298 K was passed through the tube and annulus of the heat exchanger and exhausted to the atmosphere. The inlets to the tube and annulus were connected to the gas delivery system with silicone couplings to avoid leaks. The gas flow rate was controlled using mass-flow controllers ($\pm 1.4\times10^{-3}$ mol s^{-1}). The gas flow rates in the tube and annulus were varied from 1.4×10^{-2} to 4.1×10^{-2} mol s^{-1}, in increments of 1.7×10^{-3} mol s^{-1}, which correspond to flow velocities of 0.2 to 0.7 m s^{-1} in the annulus and 0.3 to 0.9 m s^{-1} in the tube. The pressure drop was measured using a U-tube differential manometer with and without the heat exchanger in place (±9.8 Pa). The reported pressure drop across the tube, Δp_t, and annulus, Δp_{an}, is the measured pressure drop across the combined heat exchanger prototype and gas delivery system minus that of the gas delivery system.

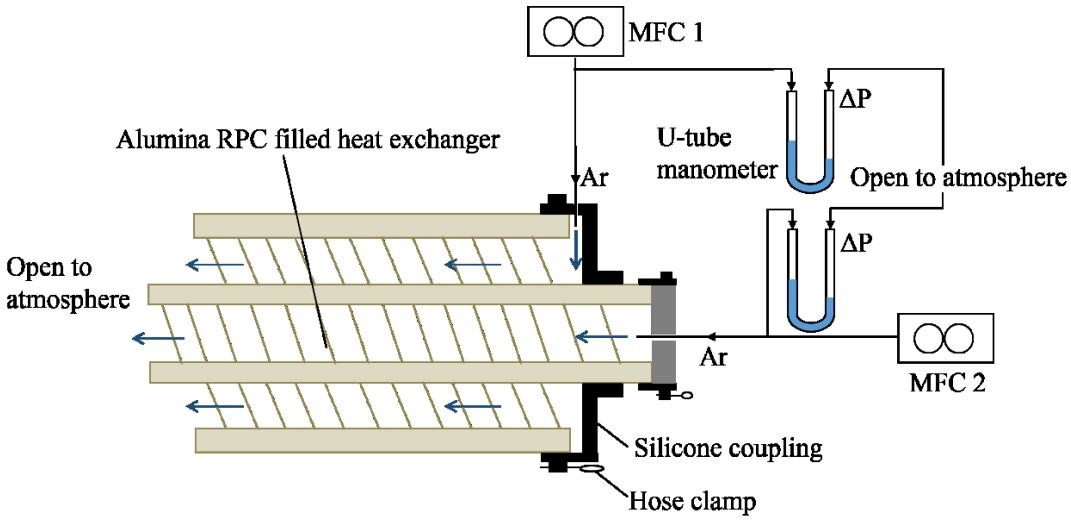

Figure 4.3 Schematic showing the experimental apparatus used to determine the permeability and inertial coefficient of the prototype. MFC = Mass flow controller.

The measured pressure drop per unit length was fit to the Darcy-Forchheimer model using MATLAB's curve-fitting toolbox to obtain the effective permeability, K_{eff}, and the inertial coefficient, F,

$$\frac{\Delta p}{L} = \frac{\mu}{K_{eff}} u + \rho F u^2 \tag{4.1}$$

The effective permeability accounts for the viscous drag due to the internal structure of the RPC plus the viscous effects of the tube,

$$K_{eff} = \left(\frac{1}{K} + \frac{1}{b}\right)^{-1} \tag{4.2}$$

where, *K* is the intrinsic permeability of the RPC and *b* is the channel permeability [56]. For steady-state, fully-developed laminar flow through a circular channel,

$$b = \frac{d_h^2}{32} \tag{4.3}$$

The permeability and inertial coefficient in the absence of pore blockage and bypass flow are estimated based on the Karman-Cozeny correlation for intrinsic permeability,

$$K = \frac{\phi^3}{k_K \tilde{a}^2} \tag{4.4}$$

and the Ergun correlation for inertial coefficient,

$$F = \frac{0.3\tilde{a}}{\phi^3} \tag{4.5}$$

For open-cell foams, the specific surface area, $\tilde{a}$, is obtained from a published correlation for high porosity (>90%) metal foam [10]. These correlations have been found to agree well with experimental results for high porosity (>90%) metal foam [10, 21] and high

porosity (80-90%) RPC [22, 57]. The values obtained from eqs (4.4) and (4.5) were also found to correlate well with experimental data provided by the manufacturer.

4.3.2 Thermal performance

The apparatus to measure the overall heat transfer coefficient, effectiveness and pressure drop is shown in figure 4.4. Hot stream inlet temperatures of 600 K and 1240 K were reached by combusting methane in air using a Meker burner [58] for air-fuel molar ratios of 23.1 and 13.4 and a fixed total flow rate of 1.7×10^{-2} mol s^{-1}. The air-fuel molar ratios were obtained by controlling the methane flow to the burner using a mass flow controller ($\pm3.4\times10^{-5}$ mol s^{-1}). The air flow was provided by a vacuum pump. The Meker burner was housed in a 95 mm o.d., 86 mm i.d. mullite tube which served as a combustion chamber. The mullite tube was connected to the inner tube of the heat exchanger using an alumina based (80% Al_2O_3, 20% SiO_2) rigid insulation plug. From the hot outlet, the gas stream containing the methane combustion products was passed through a water cooled condenser to remove water vapor and then to a laminar flow element, LFE, calibrated to ±1% of the reading. The volumetric flow rate of the dry gas through the LFE at STP (T=298K, p=1.013 bar) is

$$\dot{\forall}_{dry} = \frac{(13.03\Delta p_{LFE}^2 + 22.813\Delta p_{LFE} + 0.4296)}{\mu_{rel}}\left(\frac{298}{T_{LFE}}\right)\left(\frac{p_{LFE}}{1.013}\right) \tag{4.6}$$

where, Δp_{LFE} is the pressure drop across the laminar flow element, μ_{rel} is the viscosity of the dry gas relative to dry air at 293 K and T_{LFE} and p_{LFE} are the temperature and pressure of the gas at the LFE inlet. The viscosity of the dry gas was calculated as a molar-weighted average of each species including CO_2, CO, O_2, N_2, H_2 and CH_4,

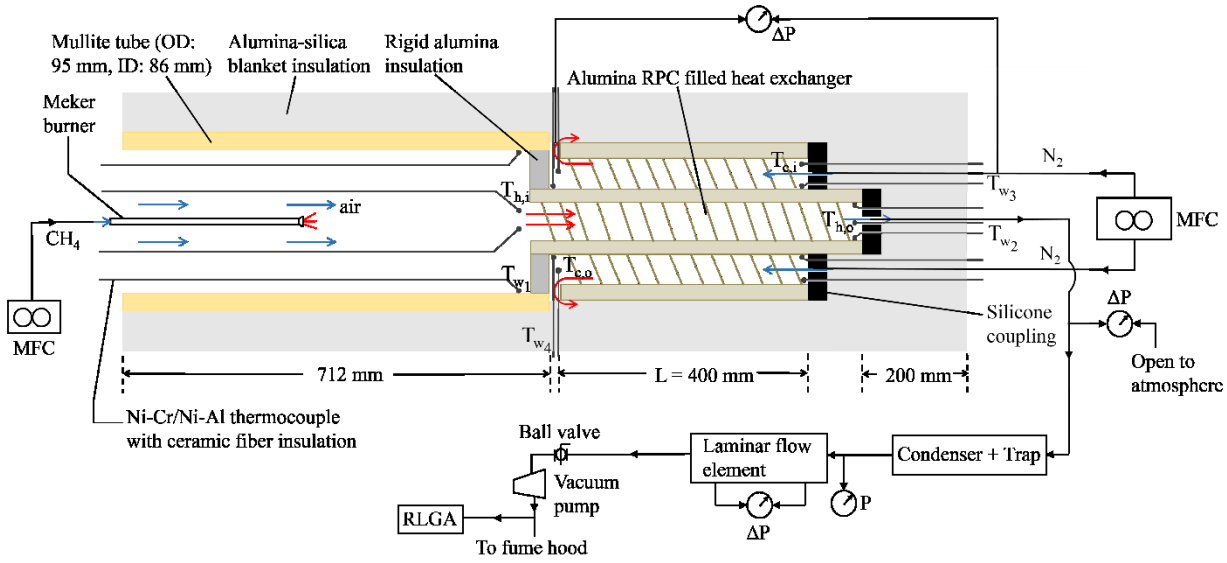

Figure 4.4 Cross-section of experimental apparatus to measure U, ε and Δp of the heat exchanger prototype. Thermocouple locations are shown with grey dots. The arrows indicate direction of gas flow. RLGA = Raman Laser Gas Analyzer

$$\mu_{dry} = \sum_{\substack{dry \\ products}} x_i \mu_i \tag{4.7}$$

The molar concentrations of CO_2, CO, O_2, N_2, H_2 and CH_4 in the outlet stream was found by passing a portion of the gas through a Raman Laser Gas Analyzer (±0.02 mol%). The remaining gas was vented to a fume hood. The molar flow rate of N_2 in the product stream is given by,

$$\dot{n}_{N_2} = x_{N_2} \dot{n}_{dry} \tag{4.8}$$

where, the molar flow rate of N_2 in the product stream equals the molar flow rate of N_2 in the reactant stream. Therefore, measuring the mole fraction of N_2 in room air, the molar flow rate of air in the reactant stream is

$$\dot{n}_{air} = \frac{\dot{n}_{N_2}}{x_{N_{2,air}}} \tag{4.9}$$

and, the total hot stream molar flow rate (CH_4+air) is

$$\dot{n}_h = \dot{n}_{air} + \dot{n}_{CH_4} \tag{4.10}$$

The root-sum-square overall uncertainty in the hot stream flow rate is ±3% for 95% confidence limit.

The nitrogen (N_2) stream flowing through the annulus was metered using a mass flow controller (±0.8% of the reading). After passing through the heat exchanger, the N_2 stream was vented. To avoid gas leaks, the cold inlet and the hot outlet were connected to the gas delivery system using silicone couplings shown in black in the figure with 0.25 in. Swagelok stainless steel tube connectors.

Chromel-Alumel (Type K, ±0.75% of reading) 14-gage thermocouples were used to measure gas temperature at the inlet and outlet of the hot ($T_{h,i}$, $T_{h,o}$) and cold ($T_{c,i}$, $T_{c,o}$) streams. Temperatures were measured at 'n' equally spaced locations along the circumference and then averaged to evaluate $T_{h,i}$, $T_{h,o}$, $T_{c,i}$ and $T_{c,o}$. For $T_{h,o}$, $T_{c,i}$ and $T_{c,o}$, n=2 and for $T_{h,i}$, n=4. At each location, the temperature was sampled at a rate of 1 kHz and time-averaged over 5 seconds. The gas temperature was obtained by correcting the thermocouple junction temperature to account for conduction along the length of the probe and radiation to and from the junction to its surroundings in accordance with the procedure outlined by Moffat [59]. The conduction error was found by treating the thermocouple as a fin with the tip at the junction temperature and the base at ambient temperature. Radiation errors were accounted for using a two-body approach where the thermocouple junction is considered to be enclosed by the surrounding walls. Type K thermocouples were used to measure wall temperatures at the hot inlet (T_{w_1}), the hot outlet (T_{w_2}), the cold inlet (T_{w_3}) and the cold outlet (T_{w_4}). At each location, wall temperature was measured at two points 180° apart and averaged. Further detail on the

uncertainty analysis and temperature corrections are provided in appendix D. The root-sum-square overall uncertainty in gas temperature measurement is ±6% for 95% confidence limit.

The pressure drop across the annulus and the tube were measured using differential capacitive pressure transducers with a full scale range of 6895 Pa and an accuracy of ±34.5 Pa.

The entire apparatus was insulated using 152 mm thick blanket of alumina-silica insulation (k=0.3 W m^{-1} K^{-1} at 1273 K). The blanket insulation extends 200 mm axially beyond the hot outlet to reduce the axial temperature gradients along the thermocouples.

Initially, a leak test was performed by flowing N_2 at the maximum flow rate of 2.7×10^{-2} mol s^{-1}. A liquid leak detector (Snoop solution by Swagelok) was applied at the joints to detect leaks. If no leaks were found, the ball valve was opened and the vacuum pump was turned on to obtain an air flow rate of 1.7×10^{-2} mol s^{-1} through the combustion chamber. The N_2 flow rate through the annulus was set to 1.8×10^{-2} mol s^{-1}. The air intake valve on the burner was kept fully open and the methane flow to the burner was lit. The methane mass flow rate was regulated till $T_{h,i}$=600 K. The temperatures, pressures and molar concentrations were monitored until they reached steady-state (±1 K over 10 mins). The N_2 flow rate was varied in increments of 3.4×10^{-3} mol s^{-1} to measure temperature and pressure drop for a range of flow rates in the annulus, 1.8×10^{-2} to 2.7×10^{-2} mol s^{-1}. The methane to air ratio was kept fixed to ensure a constant $T_{h,i}$. The experiment was repeated for $T_{h,i}$=1240 K with all other conditions being the same. The experimental conditions are summarized in Table 4.1.

Table 4.1 Experimental conditions for heat transfer and pressure drop measurements

Parameter	Value
Hot stream flow rate (CH_4 + air)	1.7×10^{-2} mol s^{-1}
Cold stream flow rate (N_2)	$1.8\times10^{-2} - 2.7\times10^{-2}$ mol s^{-1}
Air to fuel molar ratio	23.1, 13.4
Hot stream inlet temperature	600 K, 1240 K
Cold stream inlet temperature	300 K

The effectiveness of the prototype defined in terms of the energy gained by the cold stream is

$$\epsilon_c = \frac{\dot{n}_c\left(\bar{H}_c(T_{c,o}) - \bar{H}_c(T_{c,i})\right)}{\dot{n}\left(\bar{H}(T_{h,i}) - \bar{H}(T_{c,i})\right)\Big|_{min}} \tag{4.11}$$

The heat exchanger effectiveness for the hot stream is

$$\epsilon_h = \frac{\dot{n}_h\left(\bar{H}_h(T_{h,i}) - \bar{H}_h(T_{h,o})\right)}{\dot{n}\left(\bar{H}(T_{h,i}) - \bar{H}(T_{c,i})\right)\Big|_{min}} \tag{4.12}$$

The root-sum-square overall uncertainty in ε_c and ε_h are ±24% and ±4% respectively for 95% confidence limit. The difference between ε_c and ε_h is due to thermal losses to the ambient. The most appropriate measure of the heat exchanger is the cold side effectiveness. The cold side effectiveness approaches the hot side effectiveness as the R-value of the insulation is increased. The R-value is the thermal resistance of the insulation,

$$\mathrm{R-value} = \frac{\bar{T}_w - T_\infty}{\dot{Q}_{loss}} \tag{4.13}$$

where, the average wall temperature, $\bar{T}_w$, is the logarithmic mean of T_{w_4} and T_{w_2} and $\dot{Q}_{loss}$ is calculated using eq (14),

$$\dot{Q}_{loss} = \dot{n}_h c_{p,h}(T_{h,i} - T_{h,o}) - \dot{n}_c c_{p,c}(T_{c,o} - T_{c,i}) \tag{4.14}$$

The number of transfer units is defined as

$$NTU = \frac{UA}{(\dot{n}c_p)_{min}} \tag{4.15}$$

The overall heat transfer coefficient is

$$U = \frac{\dot{n}_h \left(\bar{H}_h(T_{h,i}) - \bar{H}_h(T_{h,o})\right)}{A\Delta T_{lm}} \tag{4.16}$$

where, the area for heat transfer, A, is the inner surface area of the tube and the logarithmic mean temperature difference (LMTD), ΔT_{lm}, is

$$\Delta T_{lm} = \frac{\Delta T_1 - \Delta T_2}{log(\frac{\Delta T_1}{\Delta T_2})} \tag{4.17}$$

and, $\Delta T_1 = T_{h,i} - T_{c,o}$, and, $\Delta T_2 = T_{h,o} - T_{c,i}$. The overall uncertainty in U is ±18% for 95% confidence limit.

The total thermal resistance across the heat exchanger is

$$R_{th,tot} = \frac{1}{UA} = R_{th,t} + R_{th,w} + R_{th,an} \tag{4.18}$$

The thermal resistance across the tube is given by

$$R_{th,t} = \frac{(\bar{T}_{w,h} - \bar{T}_h)}{\dot{n}_h \left(\bar{H}_h(T_{h,i}) - \bar{H}_h(T_{h,o})\right)} \tag{4.19}$$

where, the average wall temperature, $\bar{T}_{w,h}$, is the logarithmic mean of T_{w_1} and T_{w_2} and the average gas temperature, $\bar{T}_h$, is the logarithmic mean of $T_{h,i}$ and $T_{h,o}$. Similarly, the thermal resistance across the annulus is given by

$$R_{th,an} = \frac{(\bar{T}_{w,c} - \bar{T}_c)}{\dot{n}_h \left(\bar{H}_h(T_{h,i}) - \bar{H}_h(T_{h,o})\right)} \tag{4.20}$$

where, $\bar{T}_{w,c}$, is the logarithmic mean of T_{w_3} and T_{w_4} and the average gas temperature, $\bar{T}_c$, is the logarithmic mean of $T_{c,i}$ and $T_{c,o}$. The thermal resistance across the inner tube wall is given by

$$R_{th,w} = R_{th,tot} - \left(R_{th,t} + R_{th,an}\right) \tag{4.21}$$

$R_{th,t}$ and $R_{th,an}$ are overall resistances and are averaged over the length of the heat exchanger. The resistances include the resistances due to convective heat transfer from the fluid to the wall, the resistance due to conduction through the solid phase and interfacial heat transfer from the solid to the fluid and radiation in the solid phase. $R_{th,w}$ is the conductive resistance across the wall averaged over the length of the wall.

The overall heat transfer coefficient of the heat exchanger without RPC is

$$U = \left(\frac{1}{\bar{h}_t} + \frac{D_1 \log\left(\frac{D_3}{D_2}\right)}{2k_w} + \frac{D_1}{\bar{h}_{an} D_2}\right)^{-1} \tag{4.22}$$

Here, the average heat transfer coefficient in the tube, $\bar{h}_t$, is given by the Hausen correlation [60] for laminar flow in a tube with constant wall heat flux,

$$\bar{h}_t = \frac{k_h}{D_1} \times 4.36 \frac{0.036\left(\frac{Re_{D_1} Pr D_1}{L}\right)}{1 + 0.0011\left(\frac{Re_{D_1} Pr D_1}{L}\right)} \tag{4.23}$$

where, k_h is the thermal conductivity of the hot stream, μ_h is the viscosity of the hot stream evaluated at $\bar{T}_h$ and μ_w is the viscosity of the hot stream evaluated at $\bar{T}_{w,h}$. The average heat transfer coefficient in the annulus, $\bar{h}_{an}$, is given by

$$\bar{h}_{an} = \frac{k_c}{D_3 - D_2}\overline{Nu} \tag{4.24}$$

For laminar flow in an annulus with constant wall heat flux, the average Nusselt number, $\overline{Nu}$ = 6.58 for $\frac{D_2}{D_3}$ = 0.5 as published in [60].

The pumping power is given by

$$\dot{P}_{pump} = \frac{1}{\eta_{pump}}\frac{\gamma}{\gamma - 1}\dot{n}RT_i\left(\left(\frac{p_o}{p_i}\right)^{\frac{\gamma-1}{\gamma}} - 1\right) \tag{4.25}$$

where, η_{pump} is the isentropic pumping efficiency, γ is the ratio of the specific heat at constant pressure to the specific heat at constant volume for the gas, R is the universal gas constant, T_i is the gas inlet temperature to the pump, p_i is the gas pressure at the pump inlet and p_o is the pressure at the pump outlet,

$$p_o = p_i + \Delta p \tag{4.26}$$

and, Δp is the pressure drop across the heat exchanger (tube+annulus)

4.4 Results and Discussion

4.4.1 Permeability and inertial coefficient

Figure 4.5 is a plot of the measured and predicted pressure drop per unit length, *Δp/L*, as a function of the flow velocity, *u* (m s^{-1}), for the tube and annulus. The data are well correlated on the tube side by

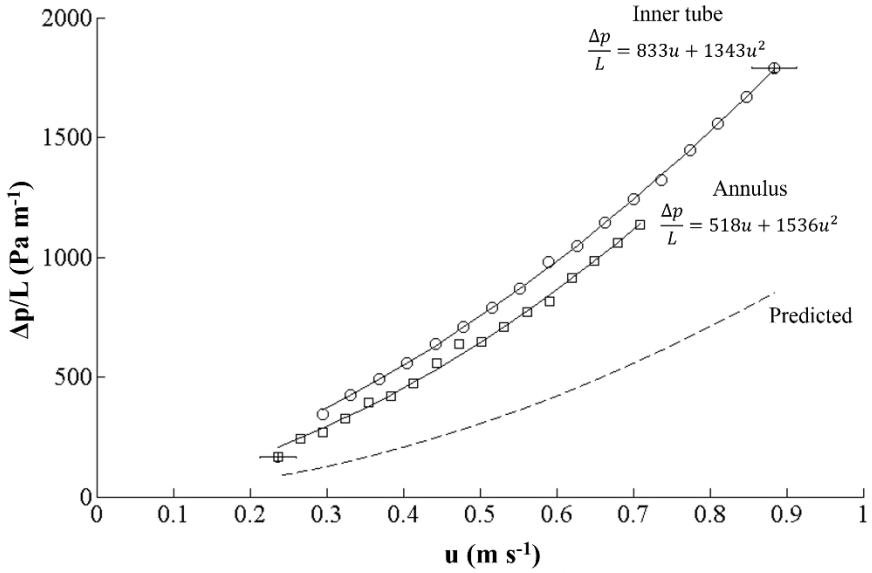

Figure 4.5 Measured and predicted pressure drop per unit length across the heat exchanger prototype with Ar as the working fluid.

$$\frac{\Delta p}{L} = 833(\pm 40)u + 1343(\pm 50)u^2 \text{ Pa m}^{-1} \tag{4.27}$$

and, on the annulus by

$$\frac{\Delta p}{L} = 518(\pm 100)u + 1536(\pm 170)u^2 \text{ Pa m}^{-1} \tag{4.28}$$

The uncertainties in the coefficients are reported for 95% confidence limit. The quadratic expressions indicate non-Darcy flow. Using eqs (4.1), (4.2) and (4.3), for the fluid properties of Ar at 298 K and 1 bar, $K = 2.5\pm0.1 \times 10^{-8}$ m^2 and $F = 810\pm30$ m^{-1} for the tube and $K = 4.1\pm0.7 \times 10^{-8}$ m^2 and $F = 925\pm100$ m^{-1} for the annulus. The higher permeability in the annulus suggests that some of the flow bypasses the RPC.

The predicted pressure drop was calculated using eq (4.1) for 80% porous, 5 ppi alumina foam. The predicted material permeability and inertial coefficient for the prototype are 1.4×10^{-7} m^2 and 555 m^{-1} respectively. The lower measured permeability is attributed to pores in the RPC blocked by the alumina slurry. The measured pressure drop

is equivalent to the predicted pressure drop across a RPC with a porosity of 61% in the tube and 66% in the annulus.

4.4.2 Thermal performance

Figure 4.6 is a plot of the overall heat transfer coefficient of the heat exchanger with and without RPC as a function of $\dot{n}_c$ at $T_{c,i}$=300±3 K, $T_{h,i}$=600±5 K, and $T_{h,i}$=1240±80 K with $\dot{n}_h$ fixed at 1.7×10^{-2} mol s^{-1}. The plot illustrates the benefits of RPC as a heat transfer surface. For the same set of experimental conditions, filling the tubes with RPC increases U by a factor of ~9.5 due to high specific surface area (917 m^{-1}). The increase in U with increase in $\dot{n}_c$ is attributed to increased convective heat transfer in the annulus as illustrated in figure 4.7 which shows the variation of thermal resistance across the heat exchanger with cold gas flow rate. The plot shows that the heat transfer is limited by the resistances in the tube ($R_{th,t}$) and annulus ($R_{th,an}$) with the wall resistance ($R_{th,w}$) an order of magnitude lower than $R_{th,t}$ and $R_{th,an}$ for the same set of operating conditions. Since $\dot{n}_h$ is fixed, $R_{th,t}$ is constant for a given hot inlet temperature and the decrease in $R_{th,tot}$ is due to the decrease in $R_{th,an}$. Increasing $\dot{n}_c$ from 1.8×10^{-2} to 2.7×10^{-2} mol s^{-1} increases Re in the annulus from 265 to 422 at $T_{h,i}$=1240 K and from 216 to 351 at $T_{h,i}$=600 K. The increase in Re corresponds to a decrease in $R_{th,an}$. The higher thermal resistances in the tube and annulus at $T_{h,i}$=600 K illustrate the effect of radiation. At $\dot{n}_h \approx \dot{n}_c$, increasing $T_{h,i}$ from 600 to 1240 K decreases $R_{th,t}$ by 17% and $R_{th,an}$ by 26.5% despite a 62% decrease in the bulk solid phase thermal conductivity of alumina from 17.6 W m^{-1} K^{-1} to 6.7 W m^{-1} K^{-1}.

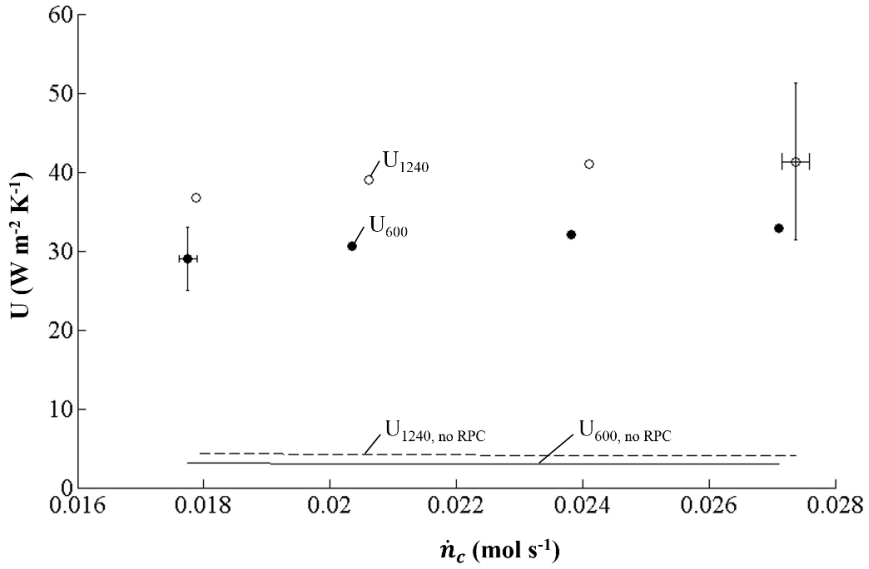

Figure 4.6 Overall heat transfer coefficient as a function of cold gas molar flow rate. The open symbols are for $T_{h,i}$ = 1240 K and the closed symbols are for $T_{h,i}$ = 600 K. The uncertainties are reported for a 95% confidence interval. The dashed line is for HX without RPC at $T_{h,i}$ = 1240 K and the solid line is for HX without RPC at $T_{h,i}$ = 600 K.

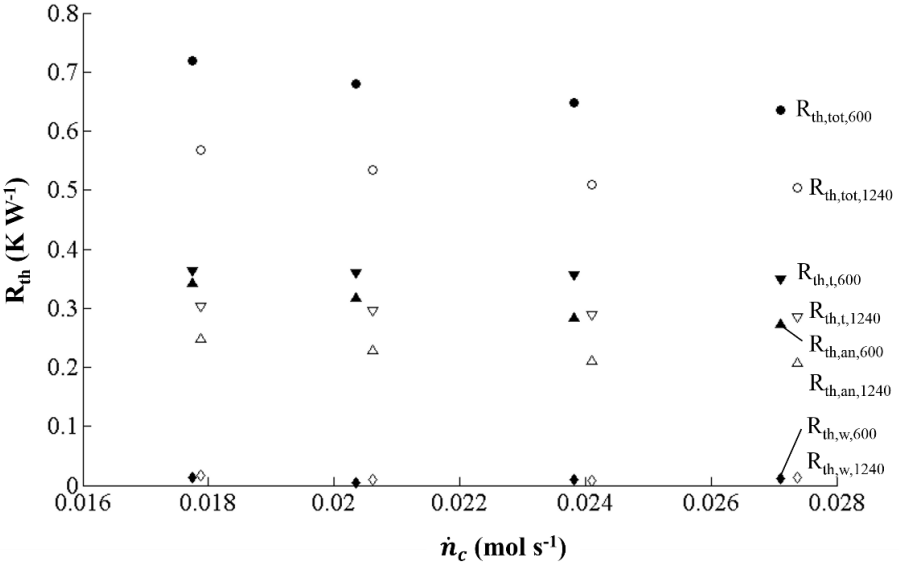

Figure 4.7 Thermal resistance as a function of cold gas molar flow rate. The open symbols are for $T_{h,i}$ = 1240 K and the closed symbols are for $T_{h,i}$ = 600 K.

Figure 4.8 shows the variation of the heat exchanger effectiveness with the number of transfer units of the prototype. The negative exponential dependence of ε_h on *NTU* is as expected for a counterflow heat exchanger [60] and can be expressed as

$$\epsilon_h = \frac{1 - e^{-NTU(1-0.64\pm0.06)}}{1 - (0.64 \pm 0.06)e^{-NTU(1-0.64\pm0.06)}} \tag{5}$$

NTU increases as $T_{h,i}$ increases from 600 to 1240 K since the total thermal resistance decreases due to radiation as discussed earlier for the same set of flow rates in the tube and annulus.

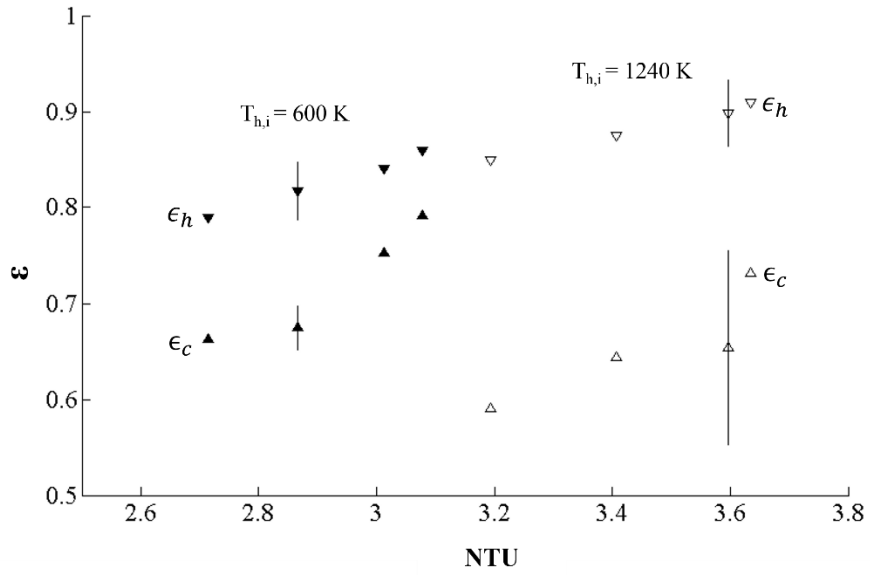

Figure 4.8 Heat exchanger effectiveness as a function of number of heat transfer units. The open symbols are for $T_{h,i}$ = 1240 K and the closed symbols are for $T_{h,i}$ = 600 K.

The ~20% difference between ε_h and ε_c is due to thermal losses through the insulation since only a portion of the energy lost by the hot stream is gained by the cold stream while the rest is lost through the insulation. Figure 4.9 is a plot of the heat flow through the hot and cold streams of the heat exchanger as a function of the cold stream flow rate. At T=1240 K, the R-value of the alumina-silica insulation as defined in eq

(4.13) used in the experiments is 0.15 m^2-K W^{-1}. As the R-value of the insulation increases, ε_c will begin to approach ε_h. Thermal losses are reduced when the hot inlet temperature decreases from 1240 K to 640 K. For $\dot{n}_c$ = 2.7×10^{-2}

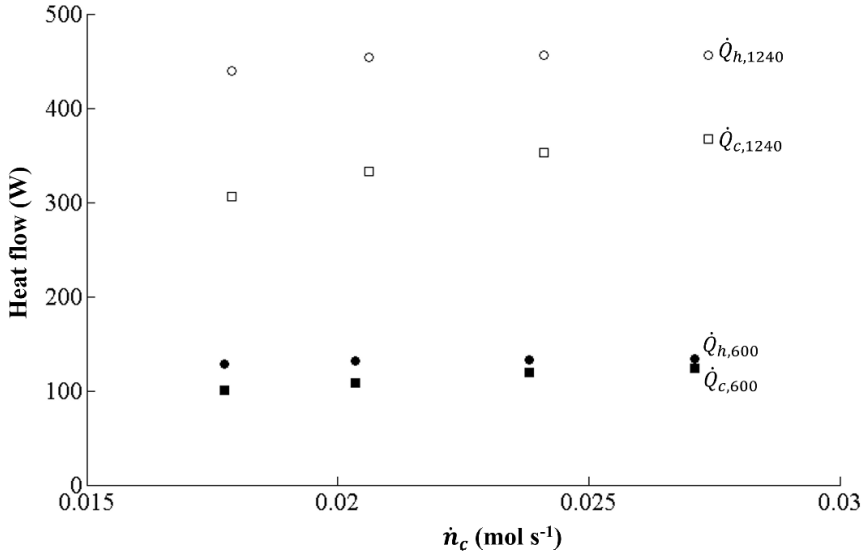

Figure 4.9 Heat flow as a function of cold stream molar flow rate. The open symbols indicate experiments run at $T_{h,i}$ = 1240 K and the closed symbols indicate experiments run at $T_{h,i}$ = 600 K.

mol s^{-1}, the ambient losses are reduced from 20% of the heat flow in the hot stream, $\dot{Q}_h$, to 8% of $\dot{Q}_h$ when reducing $T_{h,i}$ from 1240 K to 600 K. The losses are also reduced when $\dot{n}_c$ increases for a fixed hot side inlet temperature. The reduced losses are due to lower axial temperature gradients in the annulus since increasing $\dot{n}_c$ decreases the cold outlet temperature ($T_{c,o}$). As an example, at $T_{c,i}$=300 K and $T_{h,i}$=600 K, increasing $\dot{n}_c$ from 1.8×10^{-2} to 2.7×10^{-2} mol s^{-1}, decreases $T_{c,o}$ from 505±20 to 454±20 K. The cold outlet temperature decreases because the gas flow rate changes at a faster rate than the rate at which heat is transferred from the hot to the cold stream.

Figure 4.10 is a plot of the pressure drop across the heat exchanger (tube+annulus), Δp, as a function of the cold stream flow rate for a fixed hot stream flow rate of 1.7×10^{-2} mol s^{-1}. The predicted values of Δp were calculated using eq (4.1) with the values of K and F obtained in section 4.4.1. The predicted values agree to within 13% of the measured values. The measured pressure drop values indicate that no significant micro-fractures have been formed in the RPC which would lead to increased permeability of the RPC and reduced pressure drop, thus, confirming the mechanical reliability of the prototype at temperatures up to 1240 K.

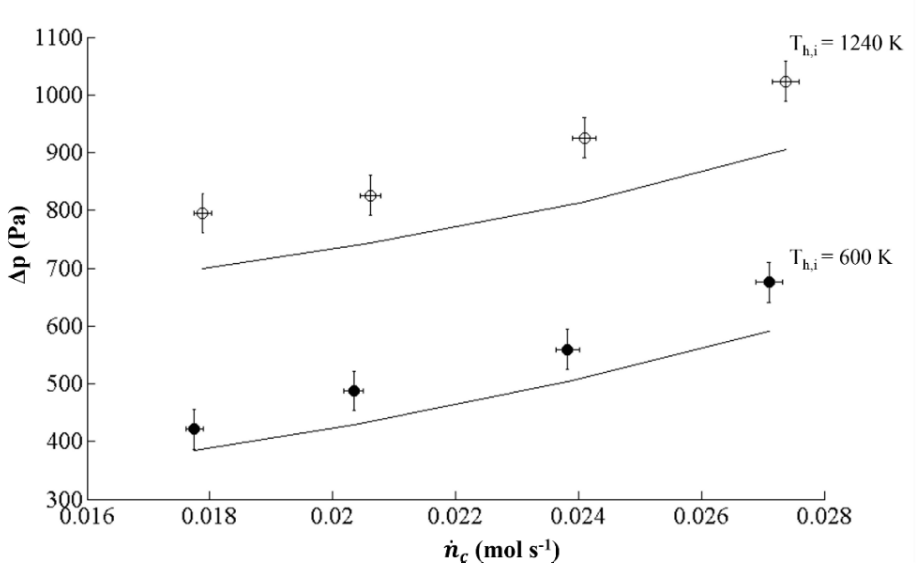

Figure 4.10 Pressure drop across the heat exchanger as a function of cold stream molar flow rate. The open symbols are for $T_{h,i}$ = 1240 K and the closed symbols are for $T_{h,i}$ = 600 K. The solid lines represent the predicted values.

The volume goodness factor plot is shown in figure 4.11. The plot shows that at 600 K and 1240 K, the heat transfer per unit heat exchanger volume ($\dot{Q}/V$) is relatively constant with increase in pumping power per unit heat exchanger volume ($\dot{P}_{pump}/V$). The trends show that over the range of Reynolds numbers tested, for a fixed hot inlet

temperature, the effect of fluid convection on heat transfer is not significant enough to outweigh the pumping power requirements with increasing flow rates.

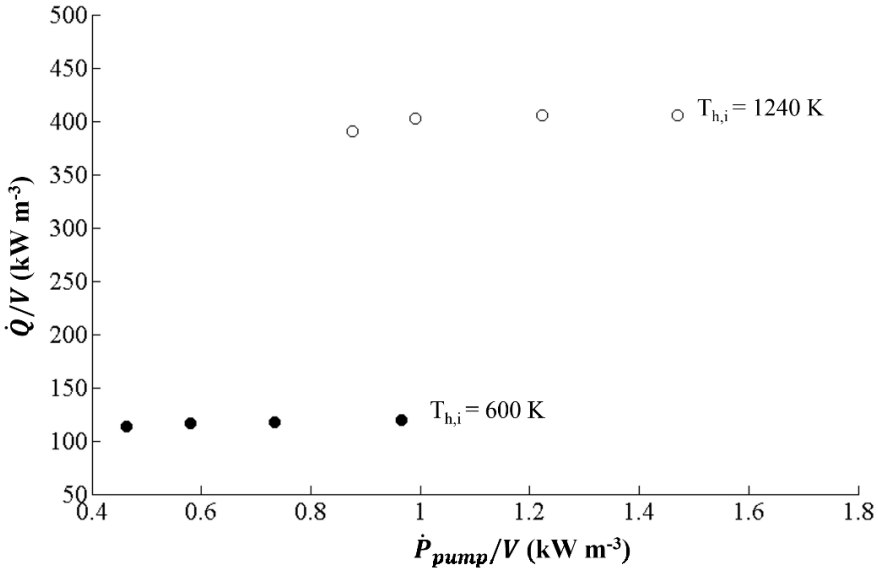

Figure 4.11 Volume goodness factor plot showing heat exchanger performance. The open symbols are for $T_{h,i}$ = 1240 K and the closed symbols are for $T_{h,i}$ = 600 K.

4.5 Conclusion

A counterflow tube-in-tube alumina RPC filled heat exchanger was fabricated and tested to measure the permeability and inertial coefficient under ambient conditions and the overall heat transfer coefficient, effectiveness and pressure drop at hot inlet temperatures of 600 K and 1240 K and cold inlet temperature of 300 K. The hot stream flow rate was constant at 1.7×10^{-2} mol s^{-1} and cold stream (N_2) flow rates varied in the range, 1.8×10^{-2} to 2.7×10^{-2} mol s^{-1}. Permeability and inertial coefficient measurements revealed that the presence of the slurry lead to some pore blockage. A portion of the flow was also found to bypass the RPC in the annulus. The heat transfer experiments showed that the measured overall heat transfer coefficient for tubes filled with RPC was ~9.5 times the value predicted when they are empty. A volume goodness factor plot was also

provided to enable direct comparison with other heat transfer enhancing media. The heat exchanger is highly compact with specific surface area of 917 m^{-1} and is reliable at temperature up to at least 1240 K obtaining overall heat transfer coefficients in the range, 36 to 41 W m^{-2} K^{-1} at 1240 K. Radiation heat transfer is significant at high temperatures with the overall heat transfer coefficient increasing by 27% from 29 to 36 W m^{-2} K^{-1} when the hot inlet temperature increases from 600 to 1240 K with all other operating conditions being the same. Cold side heat exchanger effectiveness values of up to 0.73 are obtained at hot stream molar flow rate of 1.7×10^{-2} mol s^{-1} and cold stream molar flow rate of 2.7×10^{-2} mol s^{-1}. The effectiveness can be higher still if the R-value of the insulation surrounding the heat exchanger is increased.

4.5 Impact of heat exchanger prototype performance on reactor performance

4.5.1 Permeability and inertial coefficient

The increased pressure drop measured across the heat exchanger also increases the pressure in the ceria pellet bed in the reactor. The low measured permeability and high measured inertial coefficient increases the pressure in the ceria bed by 11.5% relative to the design value of 1.28×10^{5} Pa during reduction and by 4.5% relative to the design value of 1.06×10^{5} Pa during oxidation. From the thermodynamics of ceria, for 10 ppm O_2 during reduction, the increased pressure is estimated to decrease the equilibrium fuel production by 7% relative to the fuel produced with a pressure of 1×10^{5} Pa in the ceria bed during oxidation (explained in greater detail in Appendix C). The decrease in fuel production highlights the need to reduce the pressure drop by improving the manufacturing process and decreasing the pore blockage.

4.5.1 Thermal performance

From the perspective of reactor efficiency, it is imperative to maximize the heat gained by the cold stream. The ~25% difference between ε_c and ε_h at $T_{h,i}$=1240 K can be mitigated by design of the insulation. At $T_{h,i}$=1240 K, the R-value of the alumina-silica insulation used in the experiments is 0.15 m^2-K W^{-1}. For the insulation designed for the reactor, the R-value at 1773 K is 1.64, an order of magnitude higher. Therefore, it is expected that when integrated with the reactor, the difference between ε_c and ε_h for the heat exchanger will be significantly reduced as supported by results from Bala Chandran's 2-D model [61]. The model results show that as the R-value increases from 0.15 to 1.64, for NTU=3.6, ε_c increases from 0.73 to 0.84.

The results obtained with the prototype was used to project the performance of the full-scale 1.4 m long, 85% porous, 10 ppi Al_2O_3 RPC filled heat exchanger designed for the reactor. At $T_{h,i}$=1240 K and $T_{c,i}$=298 K, over the range of cold stream flow rates tested, 1.7×10^{-2} - 2.7×10^{-2} mol s^{-1}, the measured overall heat transfer coefficient, U_m, was ~2.7 times lower than predicted by the 1-D model as shown in figure 4.12. Therefore, reducing the U_t predicted by the 1-D model by a factor of 2.7, the heat exchanger effectiveness for the designed full-scale heat exchanger was projected at $T_{h,i}$=1240 K and $T_{c,i}$=298 K for the design reduction and oxidation flow rates of 8.5×10^{-2} mol s^{-1} and 2.8×10^{-2} mol s^{-1} respectively which were beyond the range of flow rates studied experimentally. For reduction, the projected effectiveness was 0.71 and for oxidation, the projected effectiveness was 0.88, lower than the target value of 0.9. The discrepancy between the projected and target values is attributed to pore blockage, bypass flow and thermal losses through the insulation all of which is unaccounted for in the 1-D model.

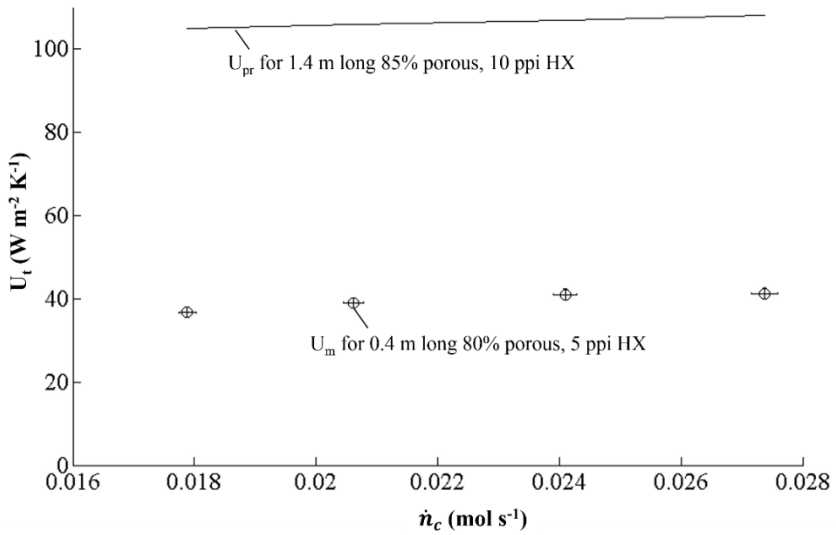

Figure 4.12 Overall heat transfer coefficient of the heat exchanger as a function of cold stream molar flow rate. The open symbols are for experiments run at $T_{h,i}$ = 1240 K. The solid line represents the predicted values from the 1-D model.

Chapter 5

Conclusion

A proposed design for a high temperature counterflow tube-in-tube alumina RPC filled heat exchanger is presented. The key challenges that are overcome by the design include the ability to operate at temperatures up to at least 1240 K and process integration with a solar thermochemical reactor.

The high temperature heat exchanger is comprised of concentric high purity (99.9%), high density alumina tubes. Alumina RPC is bonded to the tubes to significantly increase the surface area available for heat transfer. To facilitate integration with the solar thermochemical reactor, the radial dimensions of the heat exchanger are constrained to the dimensions of the reactive element preceding it. The outer tube has an o.d. of 69.9 mm and an i.d. of 63.6 mm. The inner tube has an o.d. of 44.4 mm and an i.d. of 38.1 mm. The fluid flow and heat transfer in the heat exchanger are modeled to optimize the foam morphology, namely, porosity and pore density of the RPC and the heat exchanger length. The foam morphology is selected based on a volume-averaged solution to the non-dimensional continuity, momentum and energy transport equations for fully developed flow through a homogenous and isotropic porous media. The continuity and momentum equations are solved using a radially discretized finite volume approach as outlined by Patankar [43]. The solution to the energy transport equations are based on the analytical solutions provided by Lu and Zhao et al. [12, 13]. The analytical approach makes a series of simplifying assumptions such as no thermal losses to the ambient and no axial conduction along the tube walls. The effects of natural convection and thermal dispersion are neglected and radiation heat transfer was modeled using the Rosseland

diffusion approximation. Based on the analysis presented, an alumina foam of 85% porosity and 10 ppi is found to be the optimal choice as provides a significant improvement to heat transfer ($U>150$ W m^{-2} K^{-1}) and acceptable pressure drop ($<2\times10^4$ Pa m^{-1}). The pressure drop corresponded to an estimated decrease of <5% for the equilibrium fuel production relative to the case with no pressure drop. The heat exchanger length is selected based on a coupled solution to an energy balance on the reactor and a 1-D radially lumped, finite volume model of the heat exchanger. The analysis shows that a length of 1.4 m yields the maximum reactor efficiency of 2.8% with a heat exchanger effectiveness of ~0.9 during reduction and ~0.94 during oxidation corresponding to heat duties of ~3.7 kW during reduction and ~2 kW during oxidation. The design flow rate for reduction is 8.5×10^{-2} mol s^{-1} and for oxidation is 2.8×10^{-2} mol s^{-1}. The results from the simple 1-D model was compared to a more sophisticated 2-D axisymmetric finite element model developed by Bala Chandran [42]. The resulting values of effectiveness from the two models are within 1% of each other for the same input conditions. The difference is attributed to the diffusion approximation of radiation and adiabatic boundary conditions present in the 1-D model which are absent in the 2-D model.

Neither model takes into account the impact of contact resistance at the interface between the dense alumina wall and the RPC or the impact of bypass flow. To better understand the relative importance of these effects, a shorter 0.4 m long prototype was fabricated and tested. To improve the contact resistance between the tube wall and the RPC and mitigate bypass flow, the alumina RPC is bonded to the inner alumina tube using a brazing technique similar to the one used to bond metal foams to metal tubes. The

RPC in the annulus is wrapped with a closed-cell alumina felt prior to assembly with the outer tube to attenuate bypass flow. The permeability and inertial coefficient of the prototype are evaluated by measuring the pressure drop across the heat exchanger under ambient conditions. The measured permeability was found be ~5 times lower than predicted by the 1-D model in the inner tube and ~3 times lower than predicted in the annulus. The increased permeability in the annulus suggests that some of the flow bypasses the RPC. Heat transfer and pressure drop measurements are made at elevated hot inlet temperatures of 600 K and 1240 K, a fixed cold inlet temperature of 300 K with a fixed hot stream (CH_4+air) flow rate of 1.7×10^{-2} mol s^{-1} and a range of cold stream (N_2) flow rates, 1.8×10^{-2} to 2.7×10^{-2} mol s^{-1}. Cold side heat exchanger effectiveness of up to ~0.73 is obtained at $T_{h,i}$=1240 K and up to ~0.79 at $T_{h,i}$=600 K for hot stream flow rate of 1.7×10^{-2} mol s^{-1} and cold stream flow rate of 2.7×10^{-2} mol s^{-1}. Although hot side effectiveness of up to 0.9 are obtained, the low R-value of the insulation surrounding the prototype significantly reduces the energy gained by the cold stream. However, the insulation specified for the reactor has an R-value an order of magnitude higher than the prototype insulation. It is expected that the cold side heat exchanger effectiveness will be much closer, within 7%, of the hot side values when integrated with the reactor for the same set of operating conditions namely inlet temperatures and flow rates [61]. The measured values of pressure drop are within 13% of the predicted values which indicate that no significant fractures have formed in the RPC which would lead to increased permeability and lower pressure drop. Along with the absence of any macroscopic cracks or fractures on the visible surfaces of the prototype after 15 hrs of continuous operation the agreement between the measured pressure drop and that predicted using the

permeability and inertial coefficient measured before the experiment under ambient conditions confirm the reliability of the prototype at temperatures up to 1240 K. A relation between the measured and predicted overall heat transfer coefficient of the prototype was found and used to project the performance of the full scale heat exchanger at 1240 K for the design reduction flow rate of 8.5×10^{-2} mol s^{-1} and oxidation flow rate of 2.8×10^{-2} mol s^{-1} which were beyond the range of flow rates tested. Heat exchanger effectiveness of 0.71 and 0.88 are projected during reduction and oxidation respectively, which are lower than the target value of 0.9 due to pore blockage and bypass flow in the annulus and thermal losses through the insulation.

To truly replicate the conditions in the reactor, further experiments should be performed at higher hot and cold stream flow rates representative of the reduction flow rates during reactor operation and at thermal duties beyond the present maximum of 450 W. Finally, efforts should be made to characterize the heat exchanger performance at a hot inlet temperature of 1773 K.

References

[1] Bader R., Venstrom L. J., Davidson J. H., and Lipiński W., 2013, "Thermodynamic Analysis of Isothermal Redox Cycling of Ceria for Solar Fuel Production," *Energy & Fuels*.

[2] Venstrom, L.J., De Smith, R.M., and Davidson, J.H., 2014, "Efficient splitting of CO_2 in an isothermal redox cycle based on ceria", *Energy & Fuels, American Chem. Soc.*, **28**(4), pp. 2732-2742.

[3] Hao Y., Yang C.-K., and Haile S. M., 2013, "High-temperature isothermal chemical cycling for solar-driven fuel production," Phys. Chem. Chem. Phys., **15**(40), pp. 17084–92.

[4] Panlener R. J., and Blumenthal R. N., 1975, "A thermodynamic study of nonstoichiometric cerium dioxide," J. Phys. Chem. Solids, **36**(August 1972), pp. 1213–1222.

[5] Lewinsohn, C.A., Wilson, M.A., Fellows, J.R., and Anderson, S.H., 2012, "Fabrication and joining of ceramic compact heat exchangers for process integration," *Int. J. of Applied Ceramic Technology*, **9**(4), pp. 700-711.

[6] Boomsma, K., Poulikakos, D., and Zwick, F., 2003, "Metal Foams as Compact High Performance Heat Exchangers," *Mechanics of Materials*, **35**, pp. 1161-1176.

[7] Zhang, H.Y., Pinjala, D., Joshi, K.Y., Wong, T.N., Toh, K.C., and Iyer, M.K., 2005, "Fluid Flow and Heat Transfer in Liquid Cooled Foam Heat Sinks for Electronic Packages," *IEEE Transactions on Components and Packaging Technologies*, **28**(2), pp. 272-280.

[8] ERG, 1999, "Duocel aluminum foam data sheet," ERG Material and Aerospace, Oakland.

[9] Schuetz, M.A., and Glicksmann, L.R., 1982, "Heat transfer in foam insulation," S.B.Massachusetts Institute of Technology, Cambridge, Department of Mechanical Engineering, December 1982.

[10] Bhattacharya, A., Calmidi, V.V., and Mahajan, R.J., 2002, "Thermophysical properties of high porosity metal foams," *Int. J. Heat Mass Transfer*, **45**(5), pp. 1017-1031.

[11] Lu, T.J., Stone, H.A., and Ashby, M.F., 1998, "Heat transfer in open-cell metal foams," *Acta Mater*, **46**(10), pp. 3619-3635.

[12] Lu W., Zhao C. Y., and Tassou S. A., 2006, "Thermal Analysis on Metal Foam filled Heat Exchangers. Part I: Metal Foam filled Pipes," *Int. J. Heat Mass Transfer*, **49**(15-16), pp. 2751-2761.

[13] Zhao C. Y., Lu W., and Tassou S. A., 2006, "Thermal Analysis on Metal Foam filled Heat Exchangers. Part II: Tube Heat Exchangers," *Int. J. Heat Mass Transfer*, **49**(15), pp. 2762-2770.

[14] Druma, A.M., Alam, M.K., and Druma, C., 2004, "Analysis of thermal conduction in carbon foams," *Int. J. Thermal Sci.*, **43**(7), pp. 689-695.

[15] Saadatfar, M., Arns, C.H., Knackstedt, M.A., and Senden, T., 2004, "Mechanical and transport properties of polymeric foams derived from 3D images," *Colloids Surf. andPhysicochem. Eng. Aspects*, **263**(1–3), pp. 284-289.

[16] Coquard, R., Loretz, M., and Baillis, D., 2008, "Conductive heat transfer in metallic/ceramic open-cell foams," *Adv. Eng. Materials*, **10**(4).

[17] Vafai, K., and Kim, S.J., 1990, “Fluid mechanics of the interface region between a porous medium and a fluid layer – an exact solution,” *Int. J. Heat and Fluid Flow*, **11**(3), pp. 254-256.

[18] Zhao, C.Y., Kim, T., Lu, T.J., and Hodson, H.P., 2001, “Thermal transport phenomena in porvair metal foams and sintered beds,” *Ph.D. report*, University of Cambridge, 2001.

[19] Zhao, C.Y., Kim, T., Lu, T.J., and Hodson, 2004, “Thermal transport in high porosity cellular metal foams,” *J. of Thermophysics and Heat Transfer*, **18**(3), pp. 309–317.

[20] Younis, L.B., and Viskanta, R., 1993, “Experimental determination of the volumetric heat transfer coefficient between stream of air and ceramic foam,” *Int. J. Heat and Mass Transfer*, **36**(6), pp. 1425-1434.

[21] Du Plessis, P., Montillet, A., Comiti, J., and Legrand, J., 1994, “Pressure drop prediction for flow through high porosity metallic foams,” *Chem. Eng. Sci.*, **49**, pp. 3545-3553.

[22] Petrasch, J., Meier, F., Friess, H., and Steinfeld, A., 2008, “Tomography based determination of permeability, Dupuit–Forchheimer coefficient, and interfacial heat transfer coefficient in reticulate porous ceramics,” *Int. J. Heat and Fluid Flow*, **29**, pp. 315-326.

[23] Calmidi, V.V., and Mahajan, R.L., 1999, “The effective thermal conductivity of high porosity fibrous metal foams,” *ASME J. Heat Transfer*, **121**(2), pp. 466-471.

[24] Dul’nev, G.N., and Komkova L.A., 1965, "Analysis of experimental data on the heat conductivity of solid porous systems," *J.Eng.Phys.,***9**(4), pp. 517-519.

[25] Dul'nev, G.N., 1965, "Heat transfer through solid disperse systems," *J.Eng.Phys.*,**9**(3), pp. 399-404.

[26] Russell, H.W., 1935, "Principles of heat flow in porous insulators," *American Ceramic Society Journal,* **18**, pp. 1-5.

[27] Brochhagen, F.K, and Schmidt, W., 1964, "Rigid polyurethane foams for cold insulation," *Polyurethane foams*. T.T. Healy, ed., Iliffe Books Ltd., London, pp. 121-125.

[28] Schuetz, M.A., and Glicksman, L.R., 1984, "A basic study of heat transfer through foam insulation," *Journal of Cellular Plastics,* March-April, 1984, pp.114-121.

[29] Kamiuto, K., 2008, "Modeling of composite heat transfer in open-cellular porous materials at high temperatures", *Cellular and Porous Materials: Thermal Properties Simulation and Prediction.* A. Öchsner, ed., Wiley-VCH Verlag GmbH & Co. KGaA, Weinheim, pp. 165-198.

[30] Zhao, C.Y., Lu, T.J., Hodson, H.P., and Jackson, J.D., 2004,"The temperature dependence of effective thermal conductivity of open-celled steel alloy foams," *Materials Science and Engineering*, **A 367**, pp. 123-131.

[31] Boomsma, K., and Poulikakos, D., 2001, "On the effective thermal conductivity of a three-dimensionally structured fluid-saturated metal foam," *Int. J. Heat Fluid Flow*, **44**, pp. 827-836.

[32] Bhattacharya, A., Calmidi, V.V., and Mahajan, R.L., 1999, "An analytical-experimental study for the determination of the effective thermal conductivity of high porosity fibrous foams," *Application of Porous Media Methods for Engineered Materials*, R.M. Sullivan, ed., AMD Vol. **233**, ASME, New York, pp. 13-20.

[33] Petrasch, J., Schrader, B., Wyss, P., and Steinfeld, A., 2008, "Tomography-based determination of the effective thermal conductivity of fluid-saturated reticulate porous ceramics," *ASME J. of Heat Transfer*, **130**, pp. 032602/1-032602/10.

[34] Loretz, M., Coquard, R., Baillis, D., and Maire, E., 2008, "Metallic foams: radiative properties/comparison between different models," *J. Quant. Spectrosc. Radiative Transfer*, **109**(1), pp. 16-27.

[35] Hendricks, T.J. and Howell, J.R., 1996, "Absorption / scattering coefficients and scattering phase functions in reticulated porous ceramics", *ASME J. of Heat Transfer*, **118**, pp. 79-87.

[36] Hsu, P.F., and Howell, J.R., 1992, "Measurements of thermal conductivity and optical properties of porous partially stabilized zirconia," *Experimental Heat Transfer*, **5**, pp. 293-313.

[37] Petrasch, J., Wyss, P., and Steinfeld, A., 2007, "Tomography-based Monte-Carlo determination of radiative properties of reticulate porous ceramics," *J. Quant. Spectrosc. Radiative Transfer*, **105**, pp. 180-197.

[38] Hottel, H.C., and Sarofim, A.F., 1967, *Radiative Transfer*, McGraw-Hill, New York, pp. 378-407.

[39] Glicksmann, L., Schuetz, M., and Sinofsky, M., "Radiation Heat Transfer in Foam Insulation," *Int. J. Heat and Mass Transfer*, **30**(1), pp. 187-197.

[40] Hischier, I., Hess, D., Lipinski, W., Modest, M., and Steinfeld, A., 2009, "Heat transfer analysis of a novel pressurized air receiver for concentrated solar power via combined cycles," *J. Thermal Sci. and Eng. Applications*, **1**, pp. 041002-1-6.

[41] Doermann, D., and Sacadura, J.F., 1996, "Heat transfer in open cell foam insulation," *ASME J. Heat Transfer*, **118**, pp. 88-93.

[42] Bala Chandran, R., Banerjee, A., and Davidson, J.H., 2014, "Predicted performance of a ceramic foam gas phase recuperator for a solar thermochemical reactor," *Proceedings of the ASME 2014 8th Intl. Conference on Energy Sustainability and 12th Fuel Cell Science, Engineering and Technology Conference, June 29 – July 2, 2014, Boston, Massachusetts*.

[43] Patankar, S.V., 1980, Numerical heat transfer and fluid flow, Hemisphere Publishing Corporation.

[44] Min, J.K., Jeong, J.H., Ha M.Y., and Kim, S.K., 2009, "High temperature heat exchanger studies for applications to gas turbines," *Springer Heat Mass Transfer*, **45**, pp. 175-186.

[45] Aquaro, D., and Pieve, M., 2005, "High temperature compact heat exchangers: Performance of advanced metallic recuperators for power plants," *Proceedings of 5th Int. Engineering Conference, New Jersey,* Eds. R.K. Shah, M. Ishizuka, T.M. Rudy, and V.V. Wadekar, pp. 239-246.

[46] Fend, T., Volker, W., Miebach, R., Smirnova, O., Gonsior, D., Schollgen, D., and Rietbrock, P., 2011, "Experimental investigation of compact silicon carbide heat exchangers for high temperatures," *Int. J. of Heat and Mass Transfer*, **54**, pp. 4175-4181.

[47] Schmidt, J., Scheiffele, M., Crippa, M., Peterson, P.F., Urquiza, E., Sridharan, K., Olson, L.C., Anderson, M.H., Allen, T.R., and Chen, Y., 2011, "Design, fabrication, and testing of ceramic plate-type heat exchangers with integrated flow channel design," *Int. J. of Applied Ceramic Technology*, **8**(5), pp. 1073-1086.

[48] Ponyavin, V., Chen, Y., Mohamed, T., Trabia, M., Hechanova, A.E., and Wilson, M., 2012, "Design of a compact ceramic high-temperature heat exchanger and chemical decomposer for hydrogen production," *Heat Transfer Engineering*, **33**(10), pp. 853-870.

[49] Urquiza, E., 2009, "Transient thermal, hydraulic and mechanical analysis of a counter flow offset strip fin intermediate heat exchanger using an effective porous media approach,'' *Ph.D. Thesis*, Department of Nuclear Engineering, University of California, Berkeley, pp. 113–127.

[50] Meschke, F., and Kayser, A., "Plate heat exchanger: Method for its production and its use," Patent Application DE 20090151917.

[51] Strumpf, H.J., Kotchick, D.M., and Coombs, M.G., 1982, "High-temperature ceramic heat exchanger element for a solar thermal receiver," *J. of Solar Engineering*, **104**, pp. 305-309.

[52] Knitter, R., Bauer, W., Gohring, D., and Haußelt, J., 2001, "Manufacturing of ceramic microcomponents by a rapid prototyping process chain," *Advanced Engineering Materials*, **3**(1-2), pp. 49–54.

[53] Alm, B., Imke, U., Knitter, R., Schygulla, U., and Zimmermann, S., 2008, "Testing and simulation of micro ceramic heat exchangers," *Chemical Engineering Journal*, **135S**, pp. 179-184.

[54] Sahiti, N., Durst, F., Dewan, A., 2006, "Strategy for selection of elements for heat transfer enhancement," *Intl. J. Heat and Mass Transfer*, **49**, pp. 3392-3400.

[55] Kays, W.M., London, A.L., 1998, "Compact Heat Exchangers," third reprinted ed., Krieger Publishing Company, Malabar, FL.

[56] Lage, L.J., Krueger, S.P., and Narasimhan, A., 2005, "Protocol for measuring permeability and form coefficient of porous media," *Physics of Fluids*, **17**, 088101.

[57] Richardson, J.T., Peng., Y, and Remue, D., 2000, "Properties of ceramic foam catalyst supports: pressure drop," *Applied Catalysis A: General*, **204**(1), pp. 19-32.

[58] Jenson, W.B., 2009, "The origin of the Meker and Tirrill burners," *J. Chem. Education*, **86**(12).

[59] Moffat, R.J., 1962, "Gas temperature measurement, Temperature; Its Measurement and Control in Science and Industry," **2**(1).

[60] Thirumaleshwar, M., 2009, "Fundamentals of Heat and Mass Transfer," second impression, Pearson Education, New Delhi.

[61] Bala Chandran, R., "Effect of thermal losses through insulation on cold side effectiveness," Personal Communication.

[62] Munro, R.G., 1997, "Evaluated material properties for a sintered α-alumina," *J. American Ceramic Society*, **80**(8), pp. 1919-1928.

[63] Munro, R.G., 1997, "Material properties of a sintered α-SiC," *J. Phys. Chem.*, **26**(5), pp. 1195-1203.

[64] Wang, J., Zhang, L., Zheng, Q., Vignoles, G.L., and Guette, A., 2008, "Theoretical investigation for the active-to-passive transition in the oxidation of silicon carbide," *J. American Ceramic Society*, **91**(5), pp. 1665-1673.

[65] Miller,W., 1972, "High temperature oxidation of silicon carbide", M.S. Thesis, Air Force Institute of Technology.

[66] McDaniel, A., 2012, “Solar hydrogen production with a metal oxide-based thermochemical cycle,” FY 2012 Annual Progress Report, DOE Hydrogen and Fuel Cells Program.

[67] Shigley, J.E., *Fundamentals of Mechanical Design*, Second Ed., McGraw-Hill Book Co.

[68] Kline, S.J., and McClintock, F.A., “Describing Uncertainties in Single-Sample Experiments”, Mechanical Engineering, January 1953.

[69] McAdams, W.H., *Heat Transmission*,McGraw-Hill Book Co., pp. 259, 267.

Appendix A: Effect of varying the radial dimensions of the heat exchanger on heat transfer

Although the radial dimensions of the heat exchanger (shown in figure A.1) are constrained by the dimensions of the reactive element to which it is attached, the impact of varying the radial dimensions on the thermal performance was analyzed using thermal resistances as the figure of merit. There are two resistances to heat transfer in a porous media, the resistance due to diffusion (conduction+radiation) through the solid phase and resistance due to convection between the solid and fluid phase. For a given temperature range and foam material, varying the radial dimensions of the heat exchanger affects the Reynolds number and consequently changes the resistance due to convection.

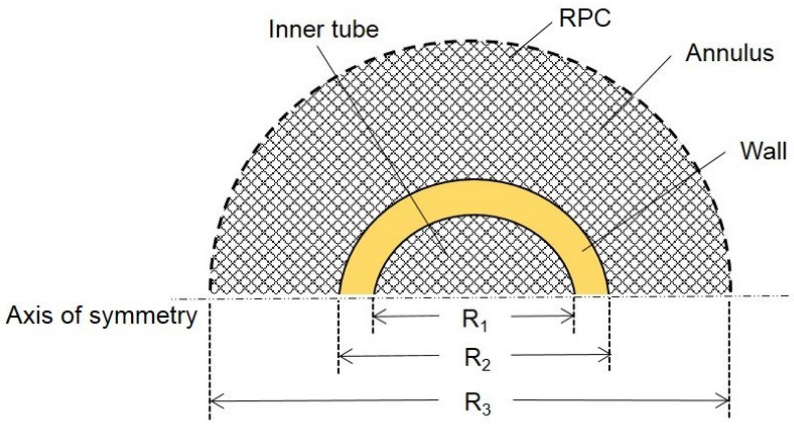

Figure A.1 Front view of the heat exchanger showing the radial dimensions.

The total thermal resistance of the heat exchanger, $R_{th,tot}$, is defined as,

$$R_{th,tot} = \frac{1}{U_t A_t} \tag{A.1}$$

where, the overall heat transfer coefficient based on the inner surface area of the tube is calculated from eq (3.12). The thermal resistance across the inner tube is given by,

$$R_{th,t} = \frac{1}{\bar{h}_t A_t} \tag{A.2}$$

and, across the annulus is given by,

$$R_{th,an} = \frac{1}{\bar{h}_{an} A_{an}} \tag{A.3}$$

where, the average heat transfer coefficients of the tube, $\bar{h}_t$, and annulus, $\bar{h}_{an}$, are calculated from eqs (3.13) and (3.15). The thermal resistance across the wall is given by an analytical solution,

$$R_{th,w} = \frac{log(\frac{R_2}{R_1})}{2\pi k_s} \tag{A.4}$$

The analysis is performed for 6 sets of inner and outer tube combinations available commercially. The radii (R_1, R_2 and R_3) and along the area ratio defined as

$$A_r = \frac{\pi(R_3^2 - R_2^2)}{\pi R_1^2} \tag{A.5}$$

for the different combinations are listed in Table A.1. The porosity and pore density are fixed at 85% and 10 ppi for the alumina RPC.

Table A.1 Radii and area ratios for the different tube combinations studied

Set #	R_1	R_2	R_3	A_r
1	19.1 mm	22.2 mm	25.4 mm	0.4
2	19.1 mm	22.2 mm	27 mm	0.6
3	19.1 mm	22.2 mm	28.6 mm	0.9
4	19.1 mm	22.2 mm	30.2 mm	1.1
5	19.1 mm	22.2 mm	31.8 mm	1.4
6	17.5 mm	20.6 mm	31.8 mm	1.9

Figure A.2 is a plot of thermal resistance versus the tube set number. With the tube thickness fixed at 6.4 mm for commercial tubes, an increase in A_r results in a decrease in R_1 and R_2 and a decrease in A_r results in a decrease in R_3 as shown in Table A.1. From the plot, it is evident that the total thermal resistance increases with an increase in the area ratio due to a decrease in the Reynolds number in the annulus. Decreasing the area ratio from 1.9 to 0.4 from set 6 to set 1 increases the Reynolds number in the annulus from 456 to 502. Consequently, the total thermal resistance decreases from 0.06 to 0.03 K W^{-1}. Thus, decreasing the area ratio to 0.4 improves the overall heat transfer coefficient by 30.7% relative to the base A_r value of 1.4.

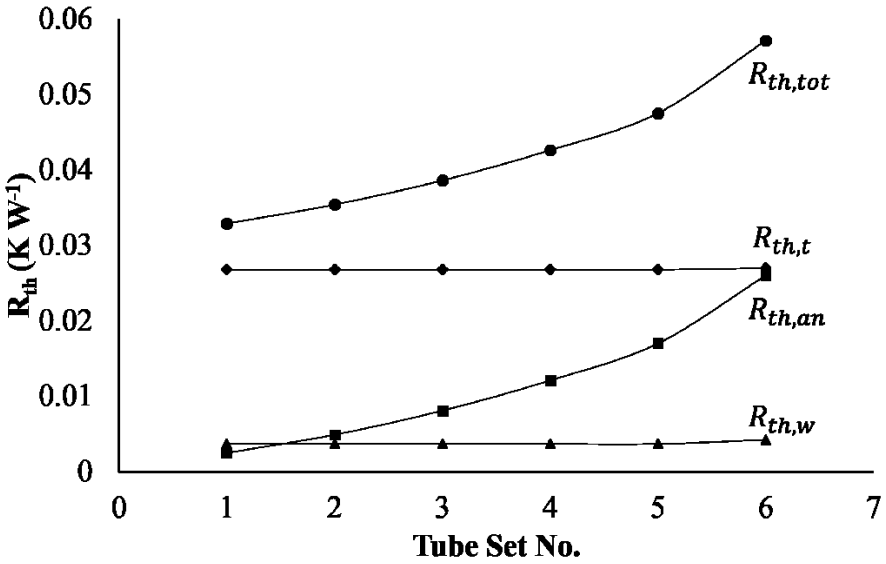

Figure A.2 Variation of thermal resistance, R_{th}, with tube set number for 85% porous, 10 ppi alumina RPC.

Appendix B: Factors precluding the use of silicon carbide in the counterflow tube-in-tube reticulate porous ceramic heat exchanger

Figure B.1 shows that the heat transfer performance is improved with an increase in the bulk solid conductivity of the RPC. Changing the RPC material from alumina, Al_2O_3 (k_s = 30 $Wm^{-1}K^{-1}$ at room temperature [62]) to silicon carbide, SiC (k_s = 187 $Wm^{-1}K^{-1}$ at room temperature [63]) would increase the overall heat transfer coefficient of the heat exchanger from ~153 $Wm^{-2}K^{-1}$ to ~337 W $m^{-2}K^{-1}$, a factor of 2.2. The increase in U with ppi also suggests that the heat transfer in SiC foams is dominated by convection as an increase in ppi increases the specific surface area available for heat transfer between the solid and fluid phases in the media whereas for alumina foams the heat transfer is dominated by radiation as discussed in section 3.2.4.1. Moreover, SiC has superior mechanical strength and creep resistance at temperatures up to 1773 K [62, 63]. Table B.1 shows a comparison of the thermo-mechanical properties of α-sintered Al_2O_3 and α-sintered SiC at 1773 K.

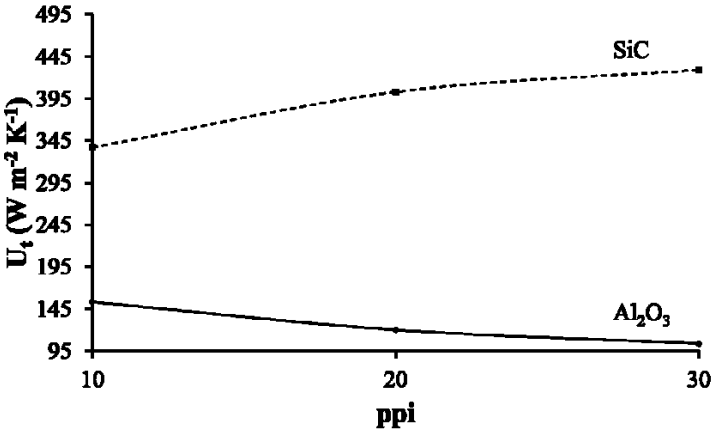

Figure B.1 Variation of overall heat transfer coefficient with pore density for 85% porous alumina (Al_2O_3) and silicon carbide (SiC) RPCs.

Table B.1 Thermal and mechanical properties of α-sintered Al_2O_3 and α-sintered SiC at 1773K

Property	**Al_2O_3**	**SiC**
Thermal conductivity	6.2 W m^{-1} K^{-1}	26.3 W m^{-1} K^{-1}
Tensile Strength	13 MPa	250 MPa
Compressive Strength	280 MPa	2700 MPa
Flexural Strength	130 MPa	446 MPa
Coefficient of thermal expansion	8.6×10^{-6} K^{-1}	5.5×10^{-6} K^{-1}

In summary, the higher thermal conductivity and improved mechanical strength makes SiC the better choice of foam material for the heat exchanger. However, the integration of an SiC heat exchanger with the solar thermochemical process of splitting CO_2 and H_2O using the redox cycling of ceria poses a few challenges.

First, the redox cycling of ceria exposes the silicon carbide foam in the heat exchanger to oxidizing atmospheres (pure O_2 during reduction and H_2O or CO_2 during oxidation) at temperatures up to 1773 K. The oxidation of SiCis categorized either as active oxidation, characterized by a mass loss, or passive oxidation, characterized by a mass gain. At relatively higher partial pressures of O_2 and temperatures (up to 1400 K), SiC 'passively' oxidizes to silica (SiO_2) and carbon monoxide (CO):

$$SiC(s) + \frac{3}{2}O_2(g) \rightarrow SiO_2(s) + CO(g) \qquad \text{(B.1)}$$

The formation of silica limits further oxidation due to its low oxygen diffusivity and acts as a protective sheath over the layer of SiC. At relatively lower partial pressures of O_2

and higher temperatures (above 1400 K), SiC is rapidly consumed to form silicon monoxide (SiO) and CO:

$$SiC(s) + O_2(g) \leftrightarrow SiO(g) + CO(g) \quad \text{(B.2)}$$

Wang et al. [64] performed thermodynamic equilibrium calculations and showed that for a partial pressure of oxygen of 7.7×10^{-6} atm, the passive oxidation of SiC, eq (B.1), is the dominant reaction up to 1320 K and the active oxidation of SiC, eq (B.2), becomes dominant at temperatures above 1420 K. The expected partial pressure of O_2 during the reduction step of the redox cycling of ceria is 10^{-5}-10^{-6} atm at a temperature of 1773 K. Thus, it is expected that SiC will 'actively' oxidize when subjected to the product stream containing pure O_2 resulting in a loss of material which will de-stabilize the foam structure and create paths for bypass flow. Moreover, Miller [65] found that water vapor strongly oxidizes SiC at temperatures above 1673 K for higher partial pressures of O_2 (0.1 – 1 atm) as is the case during the oxidation step.

An additional challenge would be the potential joining of the dense alumina tubes forming the reactive element, with the silicon carbides tubes forming the heat exchanger, since alumina (99.8% purity) tubes must be used in the reactive element section because SiC reacts vigorously with ceria at temperatures above 1673K [63]. Lewinsohn [5] identified diffusion bonding (sintering) as the most commonly used method of ceramic-ceramic bonding. However, sintering alumina and silicon carbide together at temperatures of ~1900 K is difficult as the coefficient of thermal expansion (CTE) of Al_2O_3 is ~2 times the CTE of SiC. The commonly used method for joining tubes of two different materials at room temperature is shrink-fitting. Figure B.2 illustrates the concept where two cylindrical parts are assembled by shrinking one part over the other.

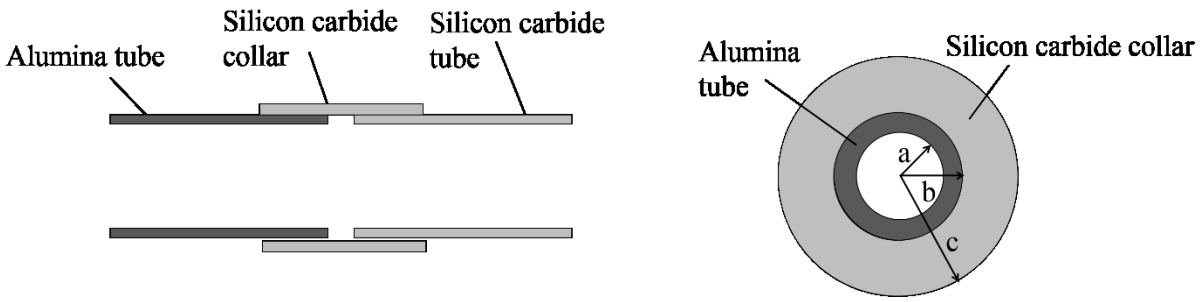

Figure B.2 Schematic of two cylindrical tubes shrink-fitted with a cylindrical collar.

A contact pressure, p, arises as a result of the assembly which causes radial and tangential stresses to develop at the contact surface. The equations for calculating the radial stress, σ_r, and the tangential stress, σ_t, are as follows,

$$\sigma_r = -p \tag{B.3}$$

$$\sigma_{it} = -p\left(\frac{b^2 + a^2}{b^2 - a^2}\right) \tag{B.4}$$

$$\sigma_{ot} = p\left(\frac{c^2 + b^2}{c^2 - b^2}\right) \tag{B.5}$$

where, σ_{it} is the tangential stress on the outer surface of the inner cylinder, σ_{ot} is the tangential stress on the inner surface of the outer cylinder, a is the inner radius of the inner cylinder, b is the outer radius of the inner cylinder and inner radius of the outer cylinder and c is the outer radius of the outer cylinder.

When the joint is heated up to 1773 K from ambient conditions (298 K), the radii of the tubes will increase due to thermal expansion according to the relation,

$$\frac{\Delta R}{R} = \alpha \Delta T \tag{B.6}$$

where, ΔR is the change in the radial dimension, R is the radius at room temperature, α is the coefficient of thermal expansion and ΔT is the change in temperature.

At 298 K, a = 19.1 mm, b = 22.2 mm for the alumina tube, and c = 24.8 mm for the silicon carbide collar. From eq (B.6), using the values of $\alpha$from Table B.1, at 1773 K, a = 19.34 mm, b = 22.48 mm and c = 25 mm. The deformation or interference, δ, is given by the difference between the increase in the outer radius of the tube and the increase in the inner radius of the collar and is equal to 0.1 mm. The deformation is related to the contact pressure by [64],

$$\delta = \frac{bp}{E_o}\left(\frac{c^2 + b^2}{c^2 - b^2} + \mu_o\right) + \frac{bp}{E_i}\left(\frac{b^2 + a^2}{b^2 - a^2} - \mu_i\right) \tag{B.7}$$

where, E_o (=380 GPa at T=1773 K [63]), μ_o(=0.156 at T=1773 K [63]) and E_i (=338 GPa at T=1773 K [62]), μ_i (=0.252 at T=1773 K [62]) are the elastic modulus and Poisson's ratio of the SiC collar and Al_2O_3 tube respectively. Substituting δ= 0.1 mm in eq (B.7) and solving for p gives p = 1.06×10^8 Pa. Thus, from eqs (B.3), (B.4) and (B.5), σ_r = - 1.06×10^8 Pa, σ_{it} = - 7.07×10^8 Pa and σ_{ot} = 9.56×10^8 Pa. The mean stress, σ_m, acting on the SiC collar is given by,

$$\sigma_m = \sqrt{\sigma_{ot}^2 + \sigma_r^2} \tag{B.8}$$

Thus, σ_m = 9.62×10^8 Pa acting in tension on the SiC collar. From Table B.1, the tensile strength of SiC at 1773 K is 2.5×10^8 Pa, ~4 times lower than the resulting mean stress due to the shrink fit joint, which leads to failure. The analysis illustrates the difficulty in joining two materials with vastly different CTEs at high temperatures.

Owing to the factors discussed above, alumina RPC was used in the heat exchanger to ensure material uniformity with the reactor cavity section and chemical inertness to oxidizing atmospheres.

Appendix C: Analyzing the effect of pressure drop across the heat exchanger on the equilibrium rates of fuel production in the reactor

The equilibrium rate of fuel production is equivalent to the non-stoichiometry swing in the ceria obtained between reduction and oxidation. The equilibrium ceria non-stoichiometry during reduction is obtained from ceria thermodynamic data given by Panlener et al [4]. Panlener et al. published equilibrium ceria non-stoichiometry (δ) values as a function of the partial pressure of oxygen (P_{O_2}) and the ceria temperature (T),

$$\Delta h^0_{O_2}(\delta) - T\Delta s^0_{O_2}(\delta) = RTlnP_{O_2} \tag{C.1}$$

In the present study, the ceria redox cycle operates under isothermally at 1773 K. The partial pressure of oxygen during reduction is given by,

$$P_{O_2,rd} = x_{O_2,rd}P_{tot} \tag{C.2}$$

For a specified composition of sweep gas ($x_{O_2,rd}$), e.g. N_2 with 10 ppm O_2, the equilibrium non-stoichiometry during reduction, δ_{rd}, depends on the total pressure in the ceria bed, P_{tot}, which, in turn, depends on the pressure drop across the heat exchanger downstream. The equilibrium ceria non-stoichiometry during oxidation, δ_{ox}, for CO_2 splitting is a function of the reactor temperature and the equilibrium partial pressure of oxygen for CO_2 dissociation given by reaction (C.3),

$$CO_2 \rightarrow CO + \frac{1}{2}O_2 \tag{C.3}$$

The equilibrium partial pressure of oxygen during oxidation ($P_{O_2,ox}$) is given by,

$$K_{eq} = \left.\frac{x_{CO}x_{O_2,ox}^{\frac{1}{2}}}{x_{CO_2}}\right|_{eq} \tag{C.4}$$

and,

$$P_{O_2,ox} = x_{O_2,ox} P_{tot} \quad \text{(C.5)}$$

where, K_{eq} is the equilibrium constant for the CO_2 dissociation reaction and is a function of the reactor temperature. Therefore, as in the case of reduction, for the fixed reactor temperature of 1773 K, $P_{O_2,ox}$ depends on the pressure in the ceria bed and in turn, on the pressure drop across the heat exchanger downstream.

As an example, the effect of the pressure drop across the heat exchanger on the equilibrium fuel production is shown for the design conditions of P_{tot} = 1.28×10^5 Pa during reduction and 1.06×10^5 Pa during oxidation (as listed in Table 3.4) relative to the base case of P_{tot} = 1×10^5 Pa during both reduction and oxidation. Figure C.1 shows the variation of ceria non-stoichiometry with partial pressure of oxygen for reactor temperature of 1773 K. From the plot, it can be seen that as P_{tot} increases from 1×10^5 Pa to 1.28×10^5 Pa during reduction, $P_{O_2,rd}$ increases from 1.01 Pa to 1.28 Pa and δ_{rd} decreases from 6.06×10^{-2} to 5.79×10^{-2}. On the other hand, during oxidation as P_{tot} increases from 1×10^5 Pa to 1.06×10^5 Pa, $P_{O_2,ox}$ increases from 1.83×10^2 Pa to 1.9×10^2 Pa and δ_{ox} decreases marginally from 2.13×10^{-2} to 2.12×10^{-2}. Therefore, the equilibrium swing in non-stoichiometry (δ_{rd} - δ_{ox}) decreases by ~6% relative to the base case of P_{tot} = 1×10^5 Pa.

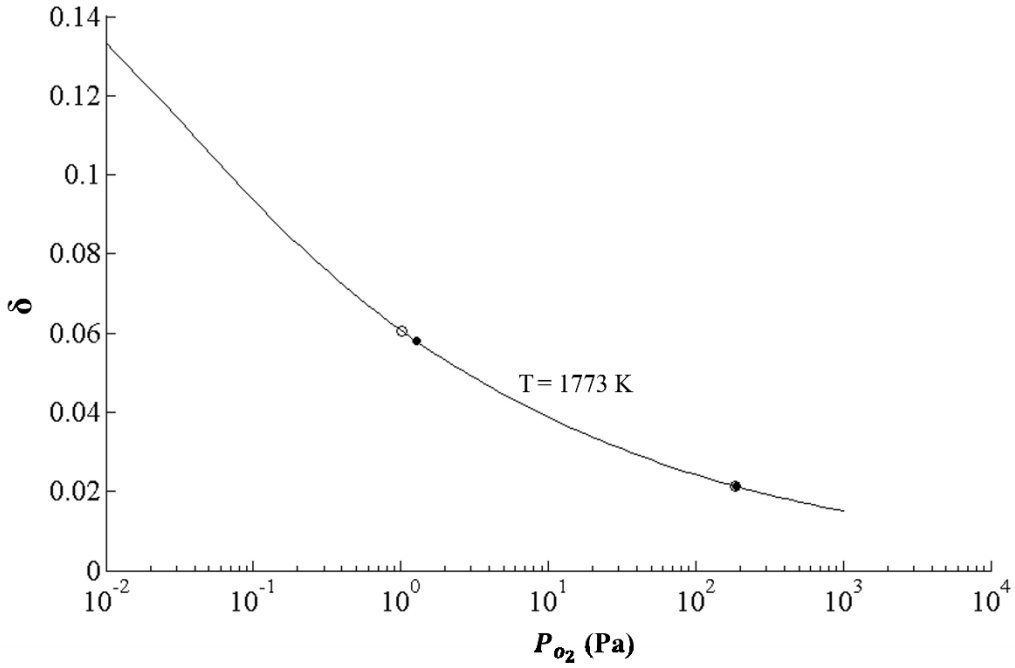

Figure C.1 Variation of ceria non-stoichiometry, δ, with partial pressure of oxygen, P_{O_2}. The open symbols are the baseline values at $P_{tot} = 1\times10^5$ Pa and the closed symbols are the values at elevated ceria bed pressures of 1.28×10^5 Pa during reduction and 1.06×10^5 Pa during oxidation.

Appendix D: Uncertainty Analysis

The uncertainty calculations are performed based on the assumption that the measured data follow a normal distribution. All of the uncertainties are reported for a 95% confidence interval. For a parameter $y=f(x_1,x_2,\ldots,x_n)$, the uncertainty in y, δy, is propagated using the root sum square (RSS) method outlined by Kline and McClintock [68],

$$\delta y = \sqrt{\left(\frac{\partial y}{\partial x_1}\delta x_1\right)^2 + \left(\frac{\partial y}{\partial x_2}\delta x_2\right)^2 + \cdots + \left(\frac{\partial y}{\partial x_n}\delta x_n\right)^2} \tag{D.1}$$

where δx_1, δx_2 and δx_n are the uncertainties in the measured values of x_1, x_2 and x_n.

D.1 Uncertainty in temperature measurement

The uncertainty in measuring wall temperature is attributed to two sources, the systematic uncertainty inherent to the thermocouple (±0.75% of the reading or ±2.2 K, whichever is greater) and the uncertainty due to spatial variations.

Since multiple thermocouple measurements are made at different spatial points at each of the locations of interest, the standard deviation of the spatial temperature variation is given by,

$$S_j = \sqrt{\frac{1}{n-1}\sum_{j=1}^{n}\left(\bar{T}_j - \bar{T}\right)^2} \tag{D.2}$$

where $\bar{T}_j$ is the mean steady temperature of each thermocouple, $\bar{T}$ is the mean temperature at the location of interest and n is the number of thermocouples at the location. The uncertainty in temperature due to spatial variations, $\delta T_{spatial}$, is given by,

$$\delta T_{spatial} = \frac{tS_j}{\sqrt{n}} \tag{D.3}$$

where t is the Student's t-distribution value for n-1 degrees of freedom and 95% confidence limits.

The total uncertainty in the measured wall temperature is calculated from the RSS of the systematic and spatial uncertainties,

$$\delta T_w = \sqrt{\delta T_{systematic}^2 + \delta T_{spatial}^2} \tag{D.4}$$

For gas temperature measurement, an additional source of uncertainty is the uncertainty in the bias correction due to radiation and conduction. For low velocity, high temperature gas measurements using bare junction thermocouples, the thermocouple junction temperature, T_j, must be corrected to account for the effects of conduction along the length of the thermocouple wire and radiation to and from the junction to its surrounding walls.

The conduction along the thermocouple can be modeled by treating it as a fin with the junction tip at T_j and the base at room temperature, T_b [59]. The steady-state difference between the gas temperature and the junction temperature due to conduction is

$$T_g = T_j + \frac{T_j - T_b}{\cosh\left(l\sqrt{\frac{4h}{dk_j}}\right)} \tag{D.5}$$

Here, l is the length of the thermocouple, d is the wire diameter and h is the convective heat transfer coefficient and is evaluated using Scadron and Warshawsky correlation [69],

$$h_c = \frac{k_f}{d} 1.122(0.085 \pm 0.009) Re_d^{0.674} Pr^{0.31} 100 < Re_d < 10000 \tag{D.6}$$

for flow parallel to the wires, and,

$$h_c = \frac{k_f}{d} 1.122(0.44 \pm 0.06) Re_d^{0.5} Pr^{0.31} 100 < Re_d < 10000 \tag{D.7}$$

for flow normal to the wires. Here, the thermocouples measuring $T_{h,o}$ and $T_{c,i}$ are parallel to the flow whilst the thermocouples measuring $T_{h,i}$ and $T_{c,o}$ are in cross-flow. Conduction along the wire is more significant for wires in parallel flow due to a lower h_c. The thermocouples at the hot outlet are therefore well insulated to reduce their axial temperature gradients.

The radiation to and from the junctions can be modeled using a simplified two-body problem approach where the junction is considered to be very small and is completely surrounded by the walls [59]. The steady-state temperature difference between T_g and T_j due to radiation is

$$T_g = T_j + \frac{\sigma \epsilon_j (T_j^4 - T_w^4)}{h_c} \tag{D.8}$$

The wall temperature is measured at two locations 180° apart at the same axial location as the junction measuring T_g as described in section 4.3.2. No correction is made to account for radiation to and from the junction measuring T_w since the circumferential variation in T_w is within ±5 K in the vicinity of the junction.

For the hot outlet, $T_{h,o}$, the conduction error dominates and eq (D.5) is used to calculate the corrected gas temperature, $T_{g,corr}$, from the mean of the measured junction temperatures. For all other inlet and outlet temperatures, $T_{h,i}$, $T_{c,o}$ and $T_{c,i}$, the error due to radiation dominates and the corrected gas temperature is obtained from eq (D.8).

Assuming zero uncertainty in the wire diameter and thermal conductivity of the junction, the uncertainty in the reported gas temperature is given by,

$$\delta T_{g,corr} = \sqrt{\delta T_w^2 + \delta h_c^2 + \left(\frac{\sigma \epsilon_j \left(T_j^4 - T_w^4\right)}{h_c} \delta \epsilon_j\right)^2} \tag{D.5}$$

Assuming zero uncertainty in the fluid thermal conductivity and the wire diameter, the uncertainty in the convective heat transfer coefficient, δh_c, is purely dependent on the uncertainty in the correlations given in eqs (D.6) and (D.7). The emissivity of the junction is taken to be 0.55±0.05 [59]. The total uncertainty in measuring gas temperature is given by,

$$\delta T_g = \sqrt{\delta T_{systematic}^2 + \delta T_{spatial}^2 + \delta T_{g,corr}^2} \tag{D.6}$$

The overall uncertainty in $T_{g,corr}$ is ±6% with the uncertainty in ϵ_j and T_w being the dominant sources.

D.2 Uncertainty in hot stream flow rate measurement

From eq (4.6) the uncertainty in the dry hot stream flow rate measured by the LFE is given by,

$$\delta \dot{n}_{dry} = \sqrt{\left(\frac{\mu_{air}}{\mu_{dry}} \delta \dot{n}_{LFE}\right)^2 + \left(\frac{\mu_{air}}{\mu_{dry}^2} \dot{n}_{LFE} \delta \mu_{dry}\right)^2} \tag{D.7}$$

Here,the uncertainty in μ_{air} is assumed to be zero. The uncertainty in the flow rate measured by the LFE, $\delta \dot{n}_{LFE}$, is ±1% and the uncertainty in the viscosity of the dry stream, $\delta \mu_{dry}$, with reference to eq (4.7), is given by,

$$\delta \mu_{dry} = \sqrt{\sum_{\substack{dry \\ products}} \mu_i \delta x_i^2} \tag{D.8}$$

Here, the uncertainty in μ_i is neglected. The uncertainty in the mole fraction of species 'i', δx_i, measured by the RLGA, is ±0.02%.Referring to eq (4.8), the uncertainty in the nitrogen flow rate in the dry stream, $\delta \dot{n}_{N_2}$, is given by,

$$\delta \dot{n}_{N_2} = \sqrt{\delta x_{N_2}^2 + \delta \dot{n}_{dry}^2} \tag{D.9}$$

where the uncertainty in the N_2 mole fraction, δx_{N_2}, measured by the RLGA is ±0.02 mol% and the uncertainty in the dry stream flow rate measured by the LFE is calculated using eq (D.7). Referring to eq (4.9),

$$\delta \dot{n}_{air} = \sqrt{\left(\frac{\delta \dot{n}_{N_2}}{x_{N_2,air}}\right)^2 + \left(\frac{\dot{n}_{N_2} \delta x_{N_2,air}}{x_{N_2,air}^2}\right)^2} \tag{D.10}$$

where the uncertainty in the N_2 mole fraction in room air, measured by the RLGA is ±0.02% and the uncertainty in the N_2 flow rate is calculated using eq (D.9). Finally, with reference to eq (4.10), the uncertainty in the total hot stream flow rate is given by,

$$\delta \dot{n}_h = \sqrt{\left(\delta \dot{n}_{CH_4}\right)^2 + (\delta \dot{n}_{air})^2} \tag{D.11}$$

The uncertainty in $\dot{n}_h$ is dominated by the uncertainty in $\dot{n}_{air}$.

D.3 Uncertainty in permeability and inertial coefficient of foam measurement

The quadratic curve fitted to the pressure drop data is of the form,

$$\frac{\Delta p}{L} = au + bu^2 \tag{D.12}$$

It is assumed that the uncertainty of the curve fit is the only uncertainty associated with the coefficients, a and b, and the actual measurement uncertainty of the pressure drop per unit length and the flow rate is nullified due to the large number of data points in the curve fit. Referring to eq (4.1), the uncertainty in the permeability is given by,

$$\delta K = \sqrt{\left(\frac{\mu}{a^2}\delta a\right)^2} \tag{D.13}$$

and the uncertainty in the inertial coefficient is given by,

$$\delta F = \sqrt{\left(\frac{\delta b}{\rho}\right)^2} \tag{D.14}$$

The uncertainty in K is ±4% for the inner tube and±17% for the annulus. The uncertainty in F is ±4% for the inner tube and ±11% for the annulus.

D.4 Uncertainty in performance metrics

With reference to eq (4.11), the uncertainty in the cold side effectiveness, $\delta\epsilon_c$, is given by,

$$\delta\epsilon_c = \epsilon_c \sqrt{\left(\frac{\delta\dot{n}_c}{\dot{n}_c}\right)^2 + \left(\frac{\delta\dot{n}_{min}}{\dot{n}_{min}}\right)^2 + \left(\frac{\delta T_{c,o}}{T_{c,o} - T_{c,i}}\right)^2 + \left(\frac{\delta T_{h,i}}{T_{h,i} - T_{c,i}}\right)^2 + \left(\frac{1}{T_{h,i} - T_{c,i}} - \frac{1}{T_{c,o} - T_{c,i}}\right)^2 \delta T_{c,i}^2} \tag{D.15}$$

where, the uncertainty in the cold stream flow rate, $\delta\dot{n}_c$, is ±0.8% of the reading and the uncertainties in $T_{c,o}$, $T_{c,i}$ and $T_{h,i}$ are calculated from eq (D.6). The uncertainty in the specific heat of the gas is assumed to be zero. The uncertainties in $T_{h,i}$ and $T_{c,o}$ are the major contributors to the uncertainty in ϵ. Referring to eq (4.12), the uncertainty in the hot side effectiveness, $\delta\epsilon_h$, is given by,

$$\delta\epsilon_h = \epsilon_h \sqrt{\left(\frac{\delta\dot{n}_h}{\dot{n}_h}\right)^2 + \left(\frac{\delta\dot{n}_{min}}{\dot{n}_{min}}\right)^2 + \left(\frac{\delta T_{h,o}}{T_{h,i} - T_{h,o}}\right)^2 + \left(\frac{\delta T_{c,i}}{T_{h,i} - T_{c,i}}\right)^2 + \left(\frac{1}{T_{h,i} - T_{h,o}} - \frac{1}{T_{h,i} - T_{c,i}}\right)^2 \delta T_{h,i}^2} \tag{D.16}$$

where, the uncertainty in the hot stream flow rate, $\delta\dot{n}_h$, is calculated from eq (D.11) and the uncertainties in $T_{h,i}$, $T_{h,o}$ and $T_{c,i}$ are calculated from eq (D.6). The uncertainty in the specific heat of the gas is assumed to be zero. The uncertainties in $\dot{n}_h$ and $T_{h,i}$ are the major contributors to the uncertainty in ϵ_h.

From eq (4.15), the uncertainty in NTU, δNTU, is given by,

$$\delta NTU = NTU\sqrt{\left(\frac{\delta\dot{n}_h}{\dot{n}_h}\right)^2 + \left(\frac{\delta U_t}{U_t}\right)^2} \tag{D.17}$$

where, the uncertainty in the hot stream flow rate, $\delta\dot{n}_h$, is calculated from eq (D.11) and the uncertainty in the overall heat transfer coefficient, U, is given by,

$$\delta U = U\sqrt{\left(\frac{\delta\dot{n}_h}{\dot{n}_h}\right)^2 + \left(\frac{\delta T_{h,i}}{T_{h,i} - T_{h,o}}\right)^2 + \left(\frac{\delta T_{h,o}}{T_{h,i} - T_{h,o}}\right)^2 + \left(\frac{\delta\Delta T_{lm}}{\Delta T_{lm}}\right)^2} \tag{D.18}$$

With reference to eq (4.17), the uncertainty in the log mean temperature difference, $\delta\Delta T_{lm}$, is given by,

$$\delta\Delta T_{lm} \tag{D.19}$$

$$= \sqrt{\left(\frac{\left(\log\left(\frac{\Delta T_1}{\Delta T_2}\right) - \frac{(\Delta T_1 - \Delta T_2)}{\Delta T_1}\right)}{\log\left(\frac{\Delta T_1}{\Delta T_2}\right)^2}\delta\Delta T_1\right)^2 + \left(\frac{\left(-\log\left(\frac{\Delta T_1}{\Delta T_2}\right) + \frac{(\Delta T_1 - \Delta T_2)}{\Delta T_2}\right)}{\log\left(\frac{\Delta T_1}{\Delta T_2}\right)^2}\delta\Delta T_2\right)^2}$$

where, $\Delta T_1 = T_{h,i} - T_{c,o}$, and, $\Delta T_2 = T_{h,o} - T_{c,i}$. The uncertainty in ΔT_{lm}, U_t and NTU are dominated by the uncertainties in $\dot{n}_h$ and $T_{h,i}$.